



**HAL**  
open science

# Clouds of Spacecraft Debris Liberated by Hypervelocity Dust Impacts on Parker Solar Probe

David Malaspina, Guillermo Stenborg, Doug Mehoke, Adel Al-Ghazwi,  
Mitchell Shen, Hsiang-Wen Hsu, Kaushik Iyer, Stuart Bale, Thierry Dudok de  
Wit

► **To cite this version:**

David Malaspina, Guillermo Stenborg, Doug Mehoke, Adel Al-Ghazwi, Mitchell Shen, et al.. Clouds of Spacecraft Debris Liberated by Hypervelocity Dust Impacts on Parker Solar Probe. *The Astrophysical Journal*, 2022, 925 (1), pp.27. 10.3847/1538-4357/ac3bbb . insu-03578706

**HAL Id: insu-03578706**

**<https://insu.hal.science/insu-03578706>**

Submitted on 17 Feb 2022

**HAL** is a multi-disciplinary open access archive for the deposit and dissemination of scientific research documents, whether they are published or not. The documents may come from teaching and research institutions in France or abroad, or from public or private research centers.

L'archive ouverte pluridisciplinaire **HAL**, est destinée au dépôt et à la diffusion de documents scientifiques de niveau recherche, publiés ou non, émanant des établissements d'enseignement et de recherche français ou étrangers, des laboratoires publics ou privés.



Distributed under a Creative Commons Attribution 4.0 International License



# Clouds of Spacecraft Debris Liberated by Hypervelocity Dust Impacts on Parker Solar Probe

David M. Malaspina<sup>1,2</sup>, Guillermo Stenborg<sup>3</sup>, Doug Mehoke<sup>3</sup>, Adel Al-Ghazwi<sup>1</sup>, Mitchell M. Shen<sup>4</sup>, Hsiang-Wen Hsu<sup>2</sup>, Kaushik Iyer<sup>3</sup>, Stuart D. Bale<sup>5,6</sup>, and Thierry Dudok de Wit<sup>7</sup>

<sup>1</sup> Astrophysical and Planetary Sciences Department, University of Colorado, Boulder, CO, USA; [David.Malaspina@colorado.edu](mailto:David.Malaspina@colorado.edu)

<sup>2</sup> Laboratory for Atmospheric and Space Physics, University of Colorado, Boulder, CO, USA

<sup>3</sup> The Johns Hopkins University, Applied Physics Laboratory, Laurel, MD, USA

<sup>4</sup> Department of Astrophysical Sciences, Princeton University, Princeton, NJ, USA

<sup>5</sup> Space Sciences Laboratory, University of California, Berkeley, CA, USA

<sup>6</sup> Physics Department, University of California, Berkeley, CA, USA

<sup>7</sup> LPC2E, CNRS, CNES, and University of Orléans, Orléans, France

Received 2021 September 20; revised 2021 November 9; accepted 2021 November 19; published 2022 January 21

## Abstract

Hypervelocity impacts on spacecraft surfaces produce a wide range of effects including transient plasma clouds, surface material ablation, and for some impacts, the liberation of spacecraft material as debris clouds. This study examines debris-producing impacts on the Parker Solar Probe spacecraft as it traverses the densest part of the zodiacal cloud: the inner heliosphere. Hypervelocity impacts by interplanetary dust grains on the spacecraft that produce debris clouds are identified and examined. Impact-generated plasma and debris strongly perturb the near-spacecraft environment, producing distinct signals on electric, magnetic, and imaging sensors, as well as anomalous behavior of the star tracker cameras used for attitude determination. From these data, the spatial distribution, mass, and velocity of impactors that produce debris clouds are estimated. Debris-cloud expansion velocity and debris fragment sizes are constrained by the observational data, and long-duration electric potential perturbations caused by debris clouds are reported, along with a hypothesis for their creation. Impact-generated plasma-cloud expansion velocities, as well as pickup acceleration by the solar wind and driven plasma waves are also measured. Together, these observations produce a comprehensive picture of near-spacecraft environmental perturbations in the aftermath of a hypervelocity impact.

*Unified Astronomy Thesaurus concepts:* Zodiacal cloud (1845); Interplanetary dust (821); Space vehicles (1549); Space debris (1542); Space plasmas (1544)

## 1. Introduction

Spacecraft throughout the heliosphere commonly experience hypervelocity impacts ( $>1 \text{ km s}^{-1}$ ) by interplanetary and interstellar dust grains. Such impacts result in the production of a transient plasma cloud through vaporization and ionization of the impactor and some fraction of the spacecraft surface material. Impact-generated plasma perturbs the spacecraft surface potential on microsecond to millisecond timescales, producing transient voltage perturbations that can be detected by electric field instruments (e.g., Gurnett et al. 1983, 1986a; Laakso et al. 1989; Tsurutani et al. 2003; Meyer-Vernet et al. 2009; Zaslavsky et al. 2012; Malaspina et al. 2014; Kellogg et al. 2016; Ye et al. 2018; Vaverka et al. 2018; Page et al. 2020; Szalay et al. 2020; Ye et al. 2020; Malaspina et al. 2020a).

The vast majority of impactors are small, with radii in the range of 10 nm to  $5 \mu\text{m}$  (e.g., Grun et al. 1985; Drolshagen et al. 2008). The physics of plasma-cloud generation by such small impactors, the resulting spacecraft potential perturbations, and the subsequent electric field instrument voltage response are topics of active research, with significant recent advances enabled by laboratory dust accelerator studies (e.g., Collette et al. 2015; Zaslavsky 2015; O’Shea et al. 2017;

Nouzák et al. 2018; Mann et al. 2019; Shen et al. 2021b and references therein). In particular, the importance of induced charging for producing observed electric field instrument voltage responses is becoming clear (Shen et al. 2021a).

A small number of impactors will be large enough (radius  $> 1 \text{ mm}$ ) to penetrate spacecraft surfaces or sever thin wire structures, creating the potential for significant damage (e.g., Lai et al. 2002; Iyer et al. 2015b; Kellogg et al. 2016; Williams et al. 2016; Sedlak & Vint 2018).

A set of impactors exists between these two extremes that may not fully penetrate spacecraft surfaces, but does liberate clouds of macroscopic spacecraft material, possibly as direct impact ejecta, possibly through spalling (Rival & Mandeville 1999). These impact-generated debris may include melt droplets and/or solid fragments such as paint chips, or multilayer insulation (MLI) fragments (Iyer et al. 2013, 2015a). Clouds of impact-generated debris may linger near the spacecraft for extended periods of time if they have slow drift velocities in the frame of the spacecraft. Such debris fragments may be large enough to scatter sunlight into scientific imager instruments and/or cause star trackers to temporarily lose the ability to produce an attitude solution. Impact-generated debris clouds were previously reported on Solar TERrestrial RELations Observatory (STEREO; St. Cyr et al. 2009; Davis et al. 2012) and Juno (Benn et al. 2017; Jorgensen et al. 2021).

This study presents observations of debris-producing dust impacts on the Parker Solar Probe (PSP) spacecraft (Fox et al. 2016), during its first eight orbits about the Sun (2018–2021).

By combining measurements of electric fields, magnetic fields, electric potentials, and scattered sunlight near the spacecraft, a comprehensive picture emerges of how debris-producing dust impacts and their resulting plasma and debris clouds influence the near-spacecraft environment, spacecraft operations, and scientific instrument measurements. In this work, observations are presented from PSP instruments and star trackers, including short-duration electric and magnetic perturbations, plasma waves driven by plasma-cloud expansion and acceleration (pickup) by the solar wind, as well as transient streaks in images. Also examined are impact-generated long-duration electric potential perturbations that persist for up to a minute (similar to observations presented by Williams et al. 2016 and Vaverka et al. 2018). This response time is  $\sim 60,000$  times longer than the electric potential perturbations created by impact-generated plasma clouds (e.g., Zaslavsky et al. 2012; Shen et al. 2021b). A hypothesis is presented for the generation of these long-duration perturbations, based on electrostatic interaction with a charged debris cloud. The spatial distribution of debris-producing impacts is examined, and is found to be consistent with impactors of approximately tens of microns in radius. Finally, the relationship between star tracker operation on PSP and debris-producing impacts is examined.

## 2. Data

This study makes use of data from the FIELDS (Bale et al. 2016) and Wide-Field Imager for Solar Probe Plus (WISPR; Vourlidas et al. 2016) instruments on PSP.

FIELDS measures electric (DC to 20 MHz) and magnetic fields (DC to 1 MHz) in situ. Electric fields are measured by five voltage-sensitive antenna elements. Four of these are long and thin (length = 2 m, diameter = 3.175 mm), extending away from the spacecraft in the plane of the heat shield in two nearly orthogonal directions. The fifth antenna is 21 cm long, oriented in the plane of the heat shield, and is located near the end of the boom on the tail of the spacecraft. Magnetic fields are measured by two fluxgate magnetometers (DC to  $\sim 146$  Hz) and one search coil magnetometer (SCM; 10 Hz to 1 MHz). The SCM is located at the tip of the magnetometer boom, nearly  $\sim 6$  m away from the heat shield.

This study makes use of FIELDS time-series data, including monopole voltage data from all five antennas and dipole voltage data from the two antenna pairs in the plane of the heat shield. The former measures the potential difference between each antenna element and the spacecraft bus “electrical ground” (e.g.,  $V_1 = V_{1\setminus\text{ant}} - V_{\text{sc}}$ ), while the latter measures the potential difference between opposing antenna elements (e.g.,  $\Delta V_{12} = V_1 - V_2$ ). The sample rate of the time-series data varies within each orbit of PSP. This study uses all continuous survey-rate time-series data recorded at a cadence fast enough to resolve dust-impact signatures ( $>50$  samples per second (Sps)). This study also uses snapshots (bursts) of high-resolution (150,000 Sps) time-series waveform data from the digital fields board (DFB). DFB burst selection algorithms are described in Malaspina et al. (2016).

WISPR (Vourlidas et al. 2016) is a white-light imager designed to measure solar photons scattered by both electron density structures in the solar wind and interplanetary dust. WISPR is mounted on the ram side of the PSP spacecraft, looking toward the interplanetary medium on the west side of the Sun when the PSP spacecraft is in its nominal solar-encounter attitude (i.e., Sun-pointed and unrolled). WISPR

consists of two telescopes, which together cover a combined radial field of view (FOV) between  $13.5^\circ$  and  $108^\circ$ . The FOV of the inner telescope (WISPR-I) extends up to  $\sim 53^\circ$  elongation, and the outer telescope (WISPR-O) starts at about  $\sim 50^\circ$  elongation. In the latitudinal direction, the FOVs of both telescopes cover  $\sim 40^\circ$ .

In order to increase the signal-to-noise ratio, WISPR images acquired during each encounter are downlinked to ground after a predetermined number of single exposures, each with exposure time  $T_s$ , are summed up on board the spacecraft. For instance, in orbit 1, the numbers of exposures were eight and 12 for the inner and outer telescopes, respectively. In subsequent orbits, these were changed to five and eight, respectively. The exposure time of each individual exposure is set according to the heliocentric distance of the PSP spacecraft. Details of the observing plans, observing modes, exposure times, etc. can be found in the WISPR calibration paper (Hess et al. 2021).

Since the downlinked images are the sum of  $N$  exposures, the time of occurrence of any given feature in the data cannot be constrained beyond the so-called “elapsed time” ( $T_{\text{el}}$ ) needed to obtain the image.  $T_{\text{el}}$  is defined as the time elapsed since the start of the first single exposure until the end of the last one. In particular, during Encounter 1, and in order to make the images from both telescopes as co-temporal as possible, each individual exposure of WISPR-I was interleaved with those of WISPR-O, resulting in an elapsed time (in particular for WISPR-I) much larger than that of the effective exposure ( $T$ ), the latter simply being  $T_s * N$ . As a consequence, this approach was discarded in subsequent orbits, and hence the observations for each telescope were taken independently from one another. This reduced the elapsed time to  $T_s * N + K$ , where  $K$  is the “dead” time resulting from the combination of the readout time of each individual exposure and the time lag between them.

Figure 1 in Malaspina et al. (2016) shows a sketch of the PSP spacecraft where the FIELDS sensors (antennas and SCM) are indicated. WISPR is the trapezoidal protrusion from the main spacecraft body just anti-sunward of the radiators, located toward the  $+X$  face (ram direction at close approach) of the spacecraft. The WISPR FOV is centered near  $+X$  in spacecraft coordinates. The star tracker cameras that provide spacecraft attitude determination are located on the anti-sunward face ( $-Z$ ) of the spacecraft, and appear in the sketch as two small cones. One star tracker FOV is oriented along  $+X$ ,  $-Z$ , and  $+Y$ , the other along  $+X$ ,  $-Z$ , and  $-Y$ .

## 3. Observations

This section presents observations of signatures of impact-generated debris clouds from FIELDS and WISPR. First, a prototypical debris-producing impact event is presented. Next, the variation in FIELDS responses to impact-generated debris clouds is presented, followed by an example of plasma waves driven by impact-generated plasma and subsequent plasma pickup by the solar wind. FIELDS debris-producing event occurrence rates and spatial locations are then explored, followed by estimates of debris fragment properties based on analysis of WISPR images and correlations between WISPR and FIELDS signatures of debris clouds. Finally, correspondence between debris-cloud signatures and star tracker demotions are presented.

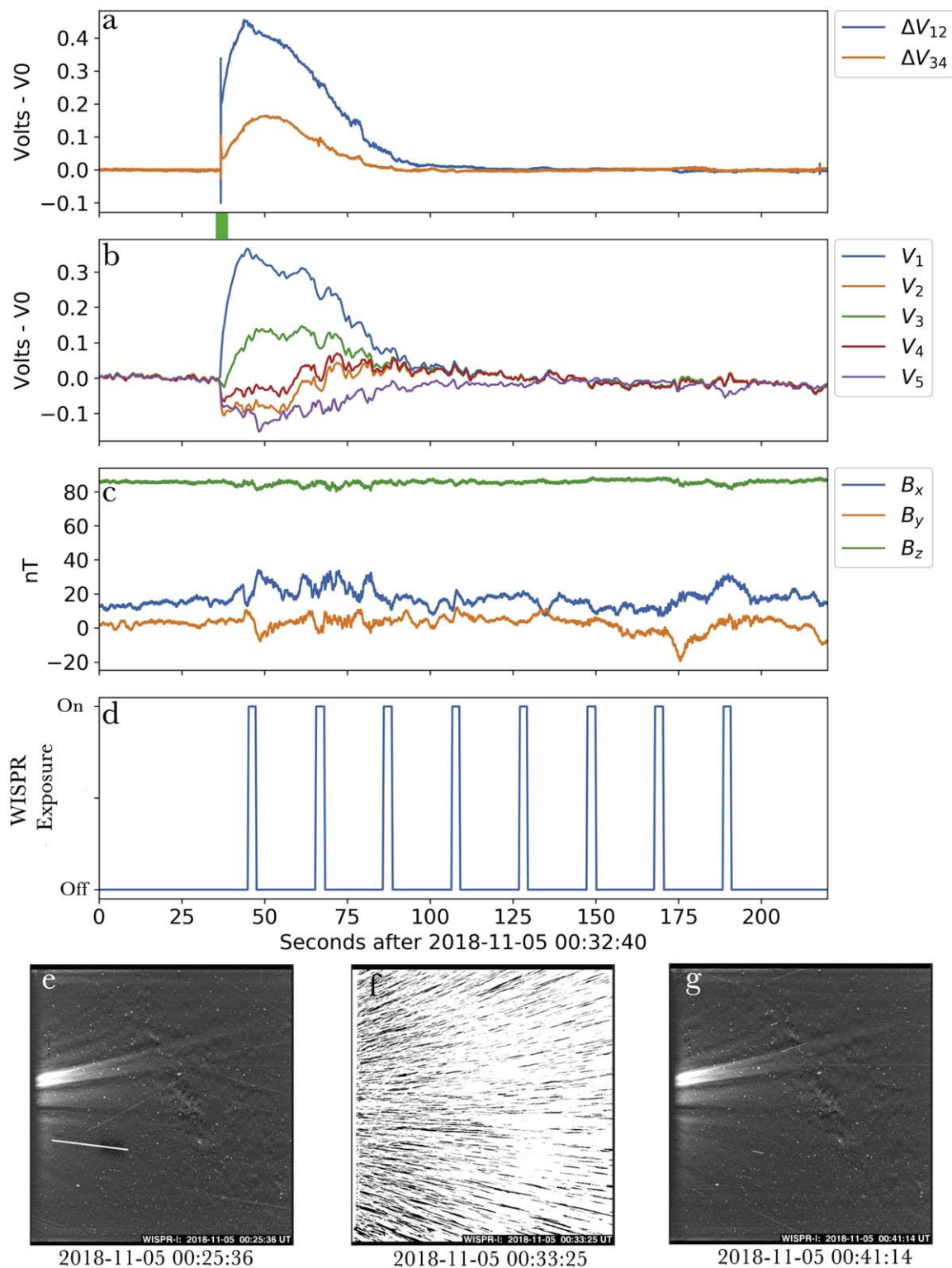


**Figure 1.** Debris-producing impact event signatures. (a) Differential voltage data from  $V_{12}$  and  $V_{34}$ . The green bar indicates the time of burst data capture (see Figure 2) (b) Monopole voltage data from  $V_1$ – $V_5$ . (c) DC-coupled magnetic field data, in spacecraft coordinates. (d) WISPR image exposures combined to produce the WISPR image in (f). WISPR inner camera images prior (e), during (f), and after (g) this impact event.

### 3.1. Example Debris-producing Impact Event

Figure 1 shows approximately 3 minutes of data recorded by FIELDS on 2018 November 5 near 00:33:17 UTC, during the first PSP perihelion pass. Figure 1(a) shows differential voltage data from the  $V_{12}$  and  $V_{34}$  antenna pairs, sampled at  $\sim 293$  Sps. Here, the DC offset (median of the first 25 s of data) has been

subtracted from each signal to enable more direct comparison between the two. The abrupt voltage spike at the start of the perturbation event is evident and is shown in more detail by Figure 2. The perturbation event itself lasts for  $\sim 1$  minute, with a maximum perturbation of  $\sim 0.42$  volts on  $V_{12}$ . The perturbation is asymmetric with respect to the two dipoles.

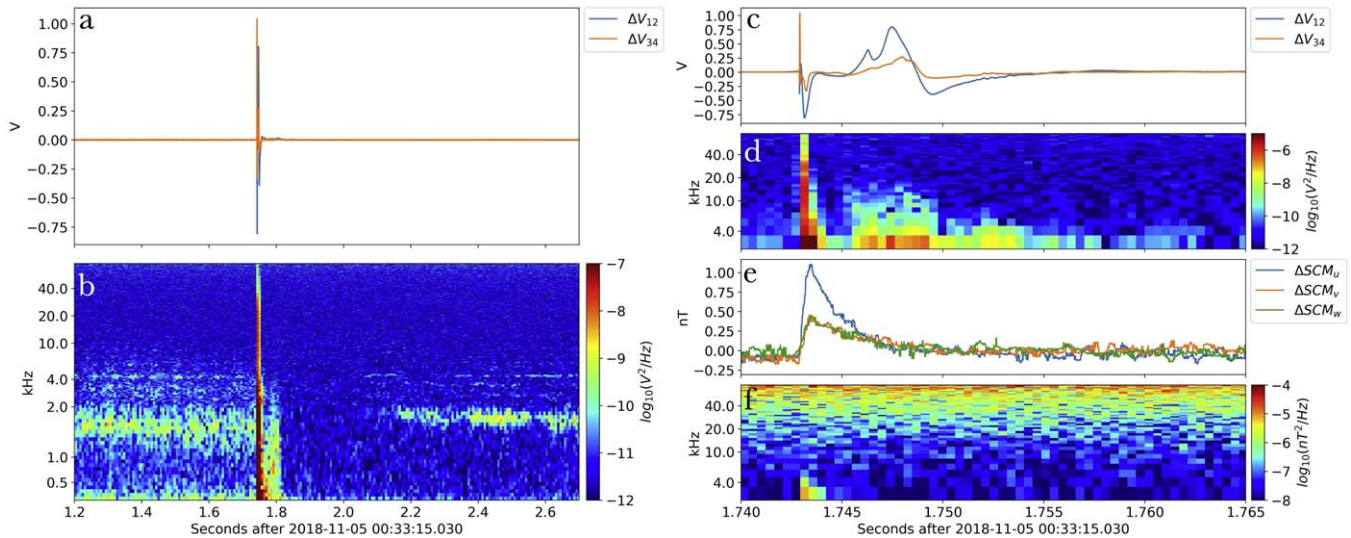


**Figure 2.** High-cadence FIELDs data for the debris-producing impact event shown in Figure 1. (a) Differential voltage data from  $V_{12}$  and  $V_{34}$ , over  $\sim 1.4$  s. (b) Windowed power spectra of data in (a). (c) Differential voltage data from  $V_{12}$  and  $V_{34}$ , over  $\sim 25$  ms. (d) Windowed power spectra of data in (c). (e) Magnetic field data in search coil instrument coordinates, over  $\sim 25$  ms. (f) Windowed power spectra of data in (e).

Figure 1(b) shows monopole data from the five voltage sensors. The slower sample rate on the monopole channels ( $\sim 2.29$  Sps) precludes observation of the potential spike associated with the impact-generated plasma cloud, but the long-duration perturbation remains clear. The perturbation is significantly different among the five voltage sensors, and is strongest on  $V_1$ , located on the ram side of the spacecraft. Figure 1(c) shows the low-frequency magnetometer data ( $\sim 293$  Sps). No clear low-frequency magnetic response is observed. The ambient plasma density at this time was  $\sim 410 \text{ cm}^{-3}$ , determined by quasi-thermal noise analysis (Moncuquet et al. 2020) near the time of the impact.

Figure 1(d) shows the timing of eight exposures that were summed to form the WISPR-I image shown in Figure 1(f). Figures 1(e) and (g) show WISPR-I images taken before and after the perturbation event. The image containing data recorded during the FIELDs perturbation event is filled with streaks of scattered light. The streaks qualitatively appear to emanate from a common point sunward of the WISPR-I FOV, suggesting a debris-cloud origin near the heat shield. Images recorded 8 minutes before and after this event show few or no debris streaks, suggesting that the debris cloud was produced and dispersed between successive WISPR images.

FIELDs captured burst waveform data at the start of this perturbation event. The extent of the burst data is indicated in Figure 1(a) as a short green bar. Figure 2(a) shows the time-series burst data for differential signals  $V_{12}$  and  $V_{34}$ . These data are AC-coupled, with a bandpass between 100 Hz and 60 kHz. Figure 2(b) shows a spectrogram of the data in 2(a). A natural plasma wave (Malaspina et al. 2020b) was observed prior to the dust-impact event, but the wave power ceases when the impact-plasma cloud is released, resuming again  $\sim 0.35$  s after the impact. This effect is interpreted as the creation of a plasma cloud so dense at antenna tip distances ( $\sim 2$  m from the heat shield) that it refracts, reflects, and/or damps ambient plasma waves to the extent that they are not detected by the antennas. This behavior is similar to plasma wave exclusion effects recorded during controlled explosion barium releases by the Active Magnetospheric Particle Tracer Explorers (AMPTE) spacecraft (Gurnett et al. 1986b; Bernhardt et al. 1987).

Figures 2(c)–(f) zoom in further on Figure 2(a), showing the differential signal detail (Figure 2(c)) and its spectrogram (Figure 2(d)), as well as the response of the three search coil axes (Figure 2(e)) and their spectrogram (Figure 2(f)). These data show that the potential perturbation due to the impact-generated plasma is highly distorted compared to the “sharp spike followed by slower recovery” behavior that is widely reported for dust-impact signatures (e.g., Zaslavsky et al. 2012). These data also show a brief impulsive magnetic field enhancement, possibly consistent with a magnetic field compression generated by the expanding impact-plasma cloud (similar to AMPTE barium release observations; Bernhardt et al. 1987).

The magnetic response peaks  $493 \mu\text{s}$  after the downward-going “preshoot” (Collette et al. 2015; Zaslavsky 2015; Mann et al. 2019) feature associated with fast electron escape. Assuming that the magnetic field perturbation is due to weak compression of the local magnetic field due to thermal pressure exerted by the expanding plasma cloud, this delay corresponds to the time required for the bulk of the impact-generated plasma cloud ions to travel from the impact location to the SCM sensor location. Assuming that the impact occurs somewhere near the heat shield, the escaping ions need to travel  $\sim 6$  m to reach the SCM. The observed time delay then corresponds to an ion plasma-cloud expansion speed of  $12.1 \text{ km s}^{-1}$ . This speed is consistent with ion cloud expansion speeds determined by hypervelocity impact laboratory experiments ( $\sim 10$ – $30 \text{ km s}^{-1}$ , Lee et al. 2012; and  $5 \text{ km s}^{-1}$  to  $15 \text{ km s}^{-1}$ , with a mean of  $\sim 10 \text{ km s}^{-1}$ , Shen et al. 2021a, 2021b). Further, the  $\sim 6$  m travel distance is an upper bound. If the impact is closer to the tail of the spacecraft, then the ion cloud expansion speed would be lower.

Finally, this event occurred  $\sim 70$  s before both PSP star trackers reported loss of attitude solution, presumably due to sunlight reflected into the anti-sunward facing star trackers by material in the debris cloud. Both star trackers went through their autonomous reset cycle and regained attitude solutions a few minutes later. The WISPR image shown in Figure 1(f) began  $\sim 10$  s after the FIELDs response to the initial impact. The only other time in the first eight orbits when both star

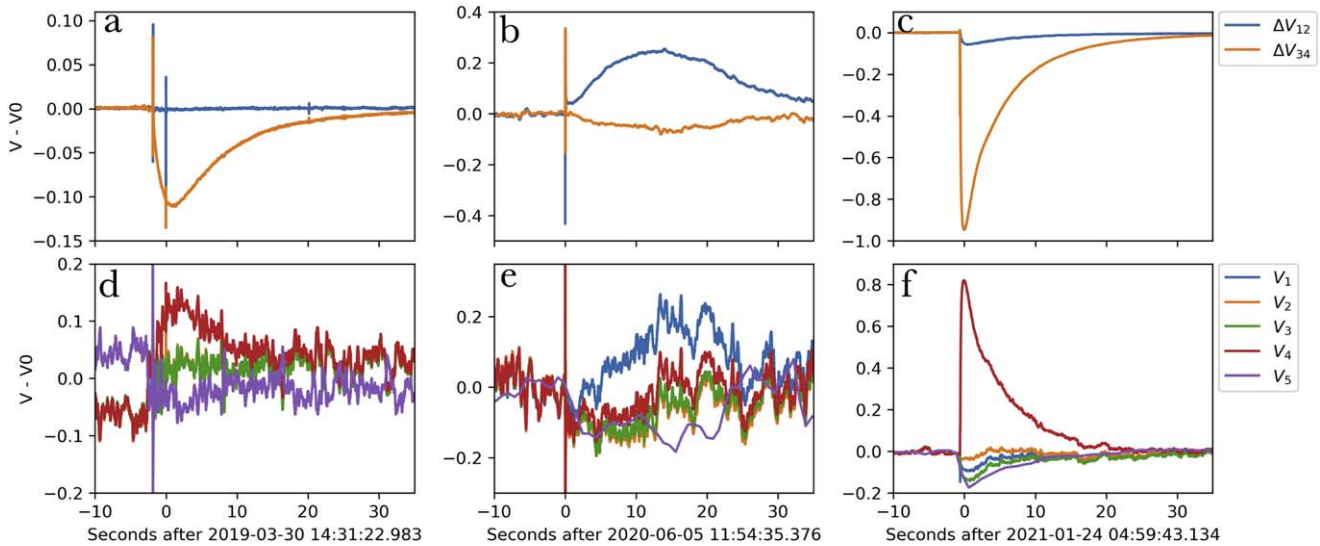


**Figure 3.** (a), (b), and (c): FIELDS dipole waveform data for three selected impact events. (d), (e), and (f): monopole waveform data for these same three impact events.

trackers were demoted simultaneously was on 2021 January 20, 05:27:23 UTC. FIELDS did register a long-duration potential perturbation event  $\sim 53$  s prior to that demotion, but there were no streaked WISPR images near in time to that demotion event (see Section 3.8).

### 3.2. FIELDS Perturbation Properties

The long-duration electric potential perturbations observed by FIELDS associated with debris-producing impact events are highly variable. Figure 3 shows three different example events, with dipole data shown in the top panels (Figures 3(a)–(c)) and monopole data in the bottom panels (Figures 3(d)–(f)). For each event, the time from impact to peak perturbation amplitude is different ( $\sim 3$ ,  $\sim 15$ , and  $\sim 1$  s). The rise time, peak amplitudes, signal decay rate, antenna showing the largest signal, and relative amplitudes on the five antennas all vary from event to event, suggesting different impact locations and debris clouds of variable shape and extent.

The FIELDS burst waveform data associated with the example event shown in Figure 2 show natural plasma wave interruption and magnetic field response in the SCM. These behaviors are interpreted in terms of an initially dense and expanding impact-generated plasma cloud. To investigate the association between these behaviors and long-duration potential perturbations, all FIELDS DFB burst data recorded during the first eight solar orbits were examined, 9849 burst captures in total.

Thirty-eight of the 240 debris-producing impact events (see Section 3.4) were captured in burst data. Of these, six showed natural plasma waves at the time of impact. All six showed plasma wave interruption similar to Figure 2. Of the 38 events debris-producing impact events captured in burst data, eight showed magnetic pulses ranging in amplitude from 0.1 to 4 nT. Four of the events with wave interruption also showed magnetic pulses. See the Appendix for a list of events considered, and their association with wave attenuation or magnetic response. This analysis supports the prior assessment that there is wide variation in FIELDS responses to debris-producing impact events.

If the observed impulsive magnetic signals, as in Figure 2(e), are magnetic field compressions driven by the expanding impact ion cloud thermal pressure, then the small  $\sim 3$ –6 m distance variation between probable impact locations along the spacecraft bus, combined with a factor-of-two uncertainty in ion cloud expansion speed from laboratory measurements (Lee et al. 2012; Shen et al. 2021a), should allow only a narrow range of time delays between dust impact and magnetic field pulse peak.

If a narrow range of time delays (expansion speeds) is observed, then the observations are consistent with an ion pressure wave interpretation for the origin of the magnetic impulsive signatures. To test this, all FIELDS DFB burst data recorded during the first eight solar orbits were examined for impulsive magnetic signatures associated with dust impacts, as in Figure 2(e). All DFB burst captures containing both differential voltage and SCM data from this interval were considered, even those without associated long-duration potential perturbations. In total, 9849 burst captures were examined. Of these, 4651 events contained dust impacts, and 61 of those contained clear impulsive magnetic responses measured by the SCM. To estimate the distribution of ion cloud expansion velocities, each impact was assumed to occur at a distance of 6 m from the SCM. Dividing this distance by the measured delay times between the dust-impact preshoot and the magnetic impulse peak produces the distribution in Figure 4. Estimated ion cloud expansion velocities are between 3.4 and 60  $\text{km s}^{-1}$ , with a median of 10.9  $\text{km s}^{-1}$ .

The primary distribution peak occurs near 10  $\text{km s}^{-1}$ , with secondary peaks near 40 and 60  $\text{km s}^{-1}$ . Because any given impact may have occurred anywhere along the spacecraft body, the distance from the impact location to the SCM may be between  $\sim 3$  and  $\sim 6$  m, and therefore the velocity estimate for any given impact may be smaller than the values in Figure 4 by at most a factor of two. Even with this uncertainty, the range of estimated plasma-cloud expansion speeds from observation is consistent with laboratory measurements (Lee et al. 2012; Shen et al. 2021a).

During orbit 1, all three SCM channels were functioning nominally, and so all three could be used to determine the

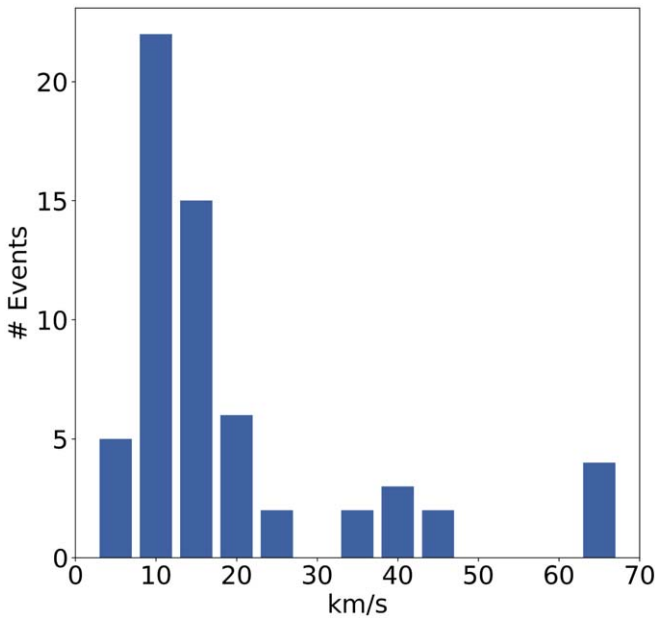


**Figure 4.** Distribution of estimated plasma-cloud expansion velocities for the 61 burst captures of dust-impact events with clear magnetic signatures from solar orbits 1 through 8, assuming 6 m between dust impact and the SCM.

magnetic field perturbation magnitude. During all subsequent encounters, only two SCM axes were functioning nominally. Therefore, these two axes were used to define the burst magnetic field magnitude after orbit 1. Because the orientation of the plasma-cloud-driven magnetic field perturbation with respect to the SCM axes is not fixed, the use of only two components increases the uncertainty in the measured time delays. A comparison during orbit 1 of time delays calculated using only two, then all three, components of the SCM produced time delay variations of  $\sim 10\%$  to  $\sim 30\%$ . Of the 61 events in Figure 4, 18 were detected during orbit 1, and so do not have this additional uncertainty.

### 3.3. Plasma Waves Driven by Impact Plasma

For some dust impacts, plasma waves below 75 kHz are observed, driven by the dense expanding plasma cloud and its acceleration (pickup) by the solar wind. Figure 5 shows an exceptionally clear example. Figure 5 shows  $\sim 40$  s of survey mode data around the debris-producing impact event, in the same format as Figures 1(a)–(c). A long-duration electric potential perturbation is evident, and is strongest on antenna V4. The dust-impact location is likely closer to the aft of the spacecraft than the event in Figure 1, because the response of V5 is stronger than any other antenna response. For this event, the debris-cloud perturbation lasts  $\sim 20$  s. The ambient plasma density for this event, determined using quasi-thermal noise analysis (Moncuquet et al. 2020), is  $142.8 \text{ cm}^{-3}$ , and the magnetic field magnitude is  $\sim 48.6$  nT. Under these conditions, the electron cyclotron frequency is  $f_{ce} = 1359.2$  Hz, the electron plasma frequency is  $f_{pe} = 107,153.9$  Hz, the upper hybrid frequency is  $f_{UH} = 107,162.5$  Hz, and  $f_{UH}/f_{ce} = 78.8$ . The  $t = 0$  time for this event is listed at the bottom of Figure 5. This time closely precedes the time of impact, but is otherwise arbitrarily selected.

Figures 5(d)–(f) shows  $\sim 0.7$  s of burst waveform data around the time of the impact, recorded at 150,000 Sps. The time-series data for the two dipole signals from the antennas in

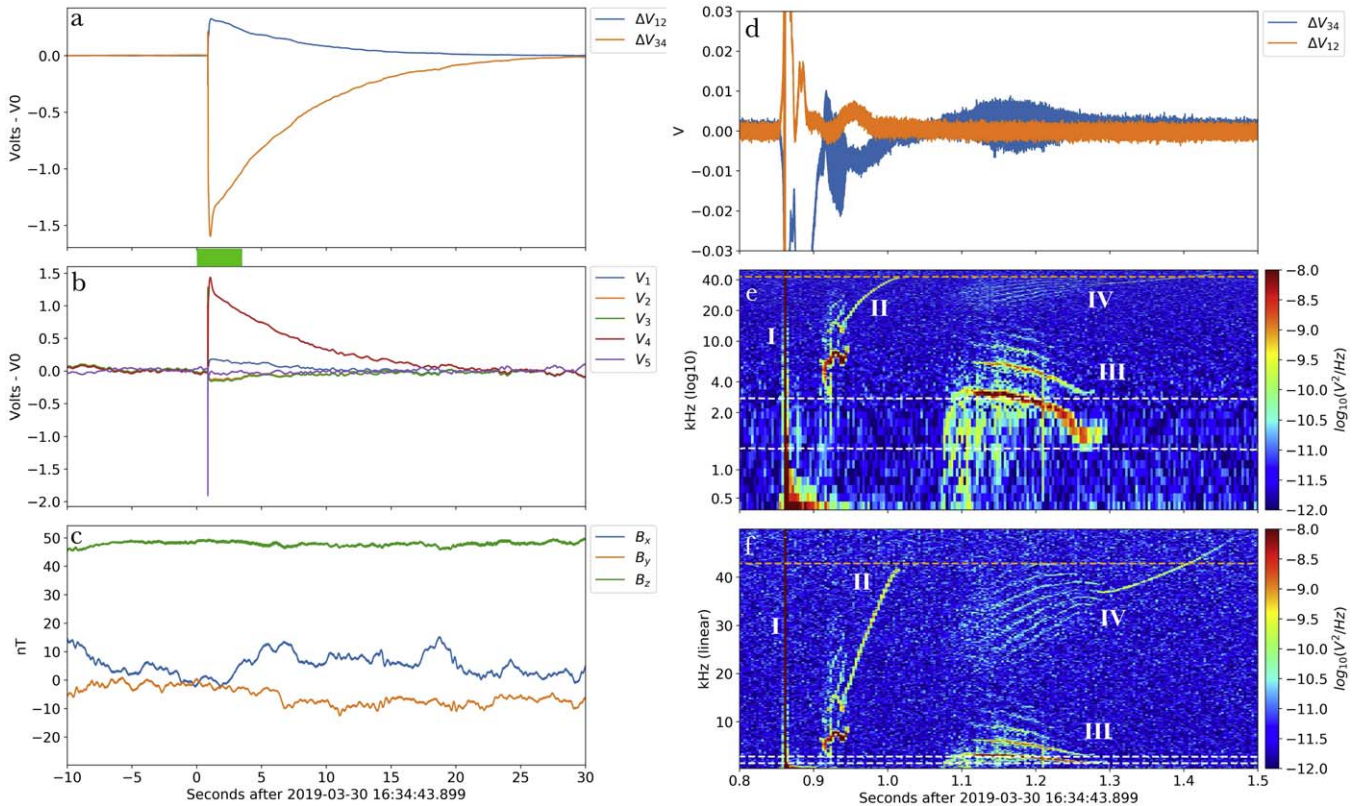
the plane of the heat shield are shown in Figure 5(d).  $\Delta V_{34}$  is plotted behind  $\Delta V_{12}$  so that the relatively more intense plasma wave signal on  $\Delta V_{34}$  is evident.

Figure 5(e) shows a spectrogram of the data in Figure 5(d). This spectrogram shows the sum of the wave power spectral density from both channels, but most of the plasma wave power is on  $\Delta V_{34}$ . The frequency axis is logarithmic. The two white dashed horizontal lines show  $f_{ce}$  and  $2f_{ce}$ . The orange dashed horizontal line shows the local electron plasma frequency (107,154 Hz), as it appears when aliased into a signal sampled at 150,000 Sps. Figure 5(f) shows the same data as Figure 5(e), but with a linear frequency axis.

Several plasma waves are present. They are labeled in both Figures 5(e) and 5(f) with upper-case Roman numerals I–IV. First is the broadband signal of the impact voltage spike (I), just before 0.9 s. Next is a rising tone between 0.9 s and 1.05 s (II). This tone stops when it reaches the aliased ambient upper hybrid frequency ( $f_{UH}$ ). We therefore interpret this signal to be a descending tone that has aliased into the observed signal range. This drifting tone is consistent with electron plasma oscillations driven at the local  $f_{pe}$  associated with the plasma-cloud density. As the cloud expands, the cloud density drops, and so the tone drops. Aliased into a signal sampled at 150,000 Sps, the tone appears to rise instead of fall. The electron plasma oscillation tone stops when the cloud density drops to the point where it is approximately equal to the ambient plasma density. At this point, a cutoff like the one observed is expected because, assuming that there are plasma oscillations associated with the cloud persisting after the cloud density drops below the ambient density, these waves will be absorbed (damped) by the ambient plasma before reaching the FIELDS antennas.

The DFB  $\Delta V$  AC-coupled channels have analog anti-aliasing filters, described in Malaspina et al. (2016). These filters are fourth-order Bessel filters with a  $-3$  dB point near 60 kHz and response that falls approximately  $\sim 60$  dB per decade of frequency above the  $-3$  dB point. Signals near 100 kHz are less than a factor of  $\sim 2$  above the  $-3$  dB frequency, and so it is reasonable to expect that sufficiently large signals between 75 kHz and 150 kHz will alias back into the observed frequency range.

The next set of waves (III) is near  $f_{ce}$ , and is most easily distinguished in Figure 5(e). These waves are consistent with electron Bernstein waves in that they (i) are always above  $f_{ce}$ , (ii) show multiple harmonics that are near, but not at, exact harmonics of one another, and (iii) show wave frequencies that drop from  $\sim 2f_{ce}$  at the start of the wave activity to  $\sim f_{ce}$  at the end of the wave activity. This last behavior in particular is consistent with electron Bernstein waves below the upper hybrid frequency  $f_{UH}$  (Nicholson 1983) driven by solar wind pickup of electrons from newly created plasma. Newly created plasma in the frame of the spacecraft will be subject to the solar wind motional electric field  $\mathbf{E} = -(\mathbf{v}_{sw} - \mathbf{v}_{sc}) \times \mathbf{B}$ . This electric field causes plasma created in the frame of the spacecraft to undergo cycloidal motion. Initially, the relative velocity  $\mathbf{v}_{sw} - \mathbf{v}_{sc}$  is large, and so too is the motional electric field. This produces a longer wavelength cycloid. As the particles accelerate, their relative velocity to the solar wind and the motional electric field magnitude drops, causing the cycloid wavelength to become shorter. The well-known dispersion relation for electron Bernstein waves below  $f_{UH}$  (Nicholson 1983) shows a transition from frequencies near  $2f_{ce}$  for long wavelengths to frequencies near  $f_{ce}$  for short



**Figure 5.** Debris-producing impact event signatures. (a), (b), (c) follow the same format as Figure 1 (a), (b), (c). (d) Differential voltage data from  $V_{12}$  and  $V_{34}$ , over  $\sim 0.7$  s. (e) Windowed power spectra of data in (a), with logarithmic frequency axis. (f) Windowed power spectra of data in (d), with linear frequency axis. White dashed lines indicate the local electron cyclotron frequency (lower) and twice the local electron cyclotron frequency (upper). The orange dashed line indicates the local electron plasma frequency as it would appear when aliased into the observed signal.

wavelengths. This behavior qualitatively matches the observations, though a more detailed study is needed to confirm this hypothesis quantitatively. If this is the physical process responsible for the drop in wave frequencies, then this event directly shows the acceleration of newly created plasma by the solar wind.

The next group of plasma waves is between 30 kHz and 40 kHz (IV). These are most clearly seen in Figure 5(f). These waves are similar to the Bernstein waves just described. Successive wave bands are spaced by near-integer multiples of  $f_{ce}$ . If these waves are electron Bernstein resonances below  $f_{UH}$ , then they correspond to harmonics in the range  $\sim 15f_{ce}$  to  $\sim 30f_{ce}$ . If these waves are electron Bernstein resonances above  $f_{UH}$  that are aliased into the observed signal, then they correspond to harmonics in the range  $f_{UH} + \sim 15f_{ce}$  to  $f_{UH} + \sim 30f_{ce}$ . The two clusters of electron Bernstein resonant waves begin and end simultaneously. A single tone (Bernstein mode) persists after all other waves have damped, though it is not clear why from the current analysis.

Ion Bernstein waves are known to be driven by the pickup of newborn ions as they are created from interstellar neutral particles within the heliosphere and are “picked up” by the solar wind motional electric field (see Joyce et al. 2012 and references therein). The initial pickup acceleration creates an agyrotropic bunching of ions in velocity space as they undergo initially cyclodial motions following their ionization. This agyrotropic bunching drives ion Bernstein waves. We propose that a similar pickup process is active in this case, accelerating impact-plasma electrons and driving electron resonant waves.

In this event, the plasma cloud is diluted to the ambient density by expansion after  $\sim 0.15$  s, and the Bernstein wave signature of plasma pickup occurs  $\sim 0.3$  s after the impact. These time delays are similar to the time after each impact where natural plasma waves are prevented from reaching the spacecraft (e.g., Figure 2(b)), consistent with the interpretation that the expanding plasma cloud is modifying the plasma environment local to the spacecraft sufficiently to prevent natural plasma waves from reaching the FIELDS antennas.

This event also has an SCM response similar to that shown in Figure 2(e). For this event, the time delay is  $1365 \mu\text{s}$ . An impact on the heat shield ( $\sim 6$  m from the SCM) therefore implies an initial cloud expansion velocity of  $\sim 4.4 \text{ km s}^{-1}$ . This is a factor-of-two slower than that derived for the event in Figure 2, but remains consistent with laboratory studies (Shen et al. 2021a).

### 3.4. Debris-cloud Occurrence Rate via FIELDS

The signature of debris-producing events in FIELDS DC-coupled electric field waveform data is distinctive: an abrupt spike followed by a  $>1$  s time period when the spacecraft potential is disturbed: rising then and gradually returning to a pre-impact level.

The FIELDS differential voltage data for the first eight orbits of PSP about the Sun (2018 October–2021 May) were searched for such signatures. The search was limited to times when the survey differential voltage data were sampled faster than 50 Sps, to ensure detection of the initial impact-plasma-cloud

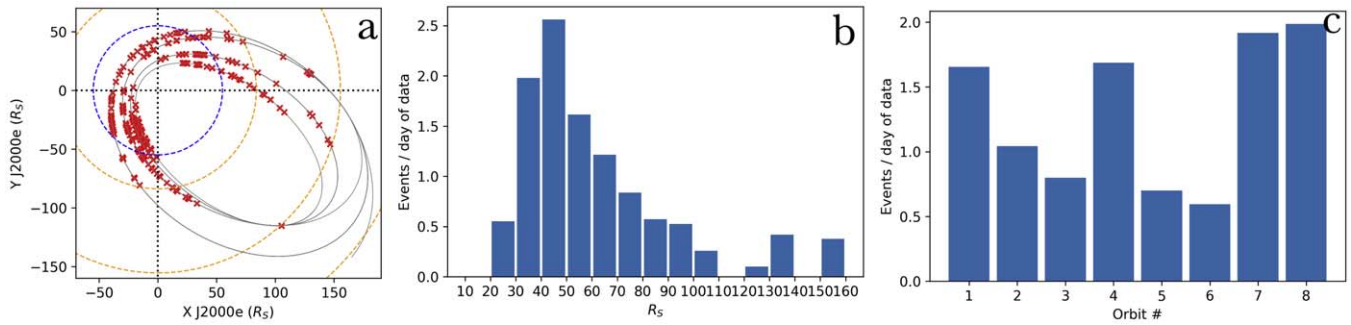


**Figure 6.** (a) Locations of FIELDS debris-producing impact detections. (b) Number of FIELDS debris-producing impact detections per day of valid data (see the text), as a function of radial distance from the Sun, for orbits 1–8. (c) Number of FIELDS debris-producing impact detections per day of valid data (see the text), as a function of orbit number.

spike. Data at this rate or faster are recorded primarily when PSP is closer than 55 solar radii ( $R_S$ ) to the Sun.

The search algorithm used is purposely designed to be inclusive of signals other than debris-cloud events, because the time-series signals associated with dust-impact-plasma clouds are highly variable (Section 3.2), and likely depend strongly on impact location (e.g., Shen et al. 2021a). The search method used is to algorithmically identify possible events, then sub-select by-eye events with signatures similar to Figure 1(a).

First, a 2 minute duration window of differential voltage data for a single antenna pair is selected. Times within 5 minutes of thruster firings or FIELDS bias sweeps are not searched. Using the data in a given window, the median value is subtracted, then the time-series data are integrated. If the data integrate to a negative value, the sign of all data is flipped to facilitate processing. The peak amplitude within the window is required to be  $>50$  mV. The data are searched for a point after the peak when they fall below  $e^{-2}$  times the peak amplitude. If such a point exists, and is more than 1 s after the peak amplitude, then the time-series data from the interval is plotted for further examination by-eye. The search window is then shifted by 30 s, and the process repeats. The  $\Delta V_{12}$  and  $\Delta V_{34}$  data were searched separately, because debris-cloud signatures can be asymmetric enough that one antenna pair may detect a given event even if the other does not.

After algorithmic selection and by-eye sub-selection, 240 unique events were found over eight orbits. The occurrence rate of these events by orbit number, by radial distance, and the locations of these events along the PSP orbit are presented in Figures 6(a)–(c), respectively. The occurrence histograms are generated by dividing the number of counts in each bin by the total time in that bin when  $>50$   $\text{sample s}^{-1}$  continuous waveform data were available, in units of days.

Figure 6(a) shows that the debris-cloud occurrence rate does not follow PSP’s orbital grouping (orbits 1, 2, and 3 were similar to one another, orbits 4 and 5 had a lower perihelion, orbits 6 and 7 had a yet lower perihelion, and orbit 8 lower still).

Figure 6(b) shows that the radial occurrence rate of debris-cloud events peaks between 40 and 50  $R_S$ , falling off sunward and anti-sunward. The maximum relative impact speed between the PSP spacecraft and  $\alpha$ -meteoroids (those on near-circular gravitationally bound orbits) is predicted to occur between 40 and 50  $R_S$  for orbits 1 to 8 (see Szalay et al. 2020, Figure 2).

Figure 6(c) shows the spatial distribution of debris-producing impact events. The PSP orbital path is shown with gray

thin lines, and the orbits of Mercury, Venus, and Earth are shown with orange dashed lines. The blue dashed line indicates 55  $R_S$ , inside of which the majority of the  $>50$  time-series sample/s data are recorded. Few debris-cloud events (indicated by red x’s) occur near perihelion. Instead, they are denser on the inbound and outbound (mostly outbound) portion of the orbit. The densest cluster (orbit 4, outbound just beyond 40  $R_S$ ) corresponds to an anomalous peak in the count rate and directionality of dust grains measured by FIELDS (Pusack et al. 2021). This peak is anomalous in the sense that existing two-component dust models cannot account for the increase in flux observed during this interval (Szalay et al. 2021).

### 3.5. WISPR Image Streaks and Occurrence Rate

As shown in Figure 1(f), some WISPR images contain streaks. These streaks are inconsistent with high-energy particle deposition in that (i) the streaks often appear to radiate outward from a fixed point out of the WISPR FOV, typically a location toward the heat shield, (ii) the streaks in some images are curved (see the Appendix), and (iii) significant variations in brightness are often observed along a given streak, including some streaks with periodically modulated intensity, consistent with tumbling debris. Based on prior experience with STEREO (St. Cyr et al. 2009; Davis et al. 2012), the streaks are assumed to be created as debris fragments liberated by dust impacts drift through the WISPR FOV and reflect sunlight into the WISPR apertures.

The WISPR instrument team assigned a quality factor (QF) to each image to indicate the amount of streaking. QF values range from 0 (no streaking) to 9 (heavily streaked). Odd values are used for images where the streaks appear to propagate radially outward from a common origination point. Even values are used for images where a significant number of streaks do not have a common origination point (including streaks with curved trajectories; see the Appendix). QF values are subjectively assigned by visual inspection of the images. Figure 7 shows representative images for each QF value. Images with  $QF \geq 5$  show high densities of streaks.

### 3.6. WISPR Streak Analysis

An analysis of streaks in WISPR images was carried out to estimate the basic properties of the fragments causing them. For this analysis, it is important that WISPR is designed to look at quasi-stationary, far-off objects, and all streak-producing fragments are well within the blur distance of the optical

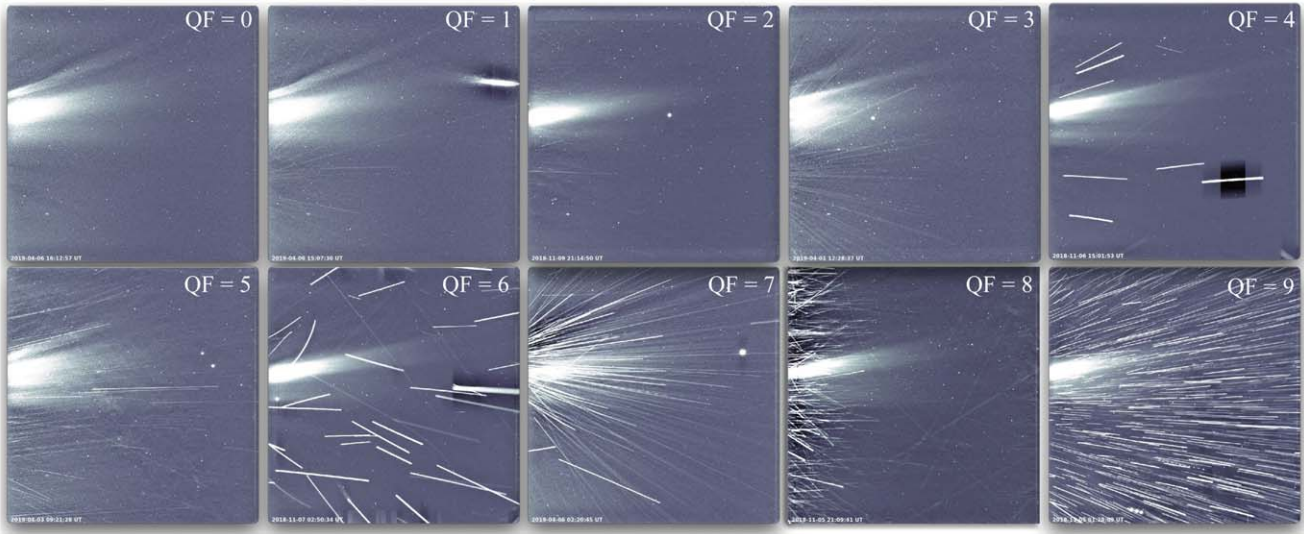


**Figure 7.** WISPR images showing examples for each quality flag (QF) value.

system. Also, WISPR images often capture events seconds to minutes after a given impact.

Streaks are caused by fragments of different sizes and velocities moving across the WISPR FOV and scattering or reflecting light into the aperture. These fragments are not resolved by the imager, so each can be assumed to be a point source. Solar photons reflect off the fragments and enter the WISPR detector for the time period that the fragment is in the FOV. The resulting streak width is a function of the particle distance from the aperture. The streak intensity is a function of the particle size, speed, and the distance to the Sun at the time of observation. The deposited photon energy associated with the streak can be computed directly from the mean solar brightness (MSB) values of the images and the known conversion factors specific to the WISPR optical design (Vourlidis et al. 2016).

Eighteen images with well-defined streaks are analyzed, six from Encounter 1, and 12 from Encounter 2. The average WISPR QF for the six Encounter 1 images was  $4.7 \pm 2.9$ . There were a total of 682 streaks in the images, of which 22 were analyzed in detail. The average QF for the 12 images of Encounter 2 was  $5.4 \pm 2.5$ . There were a total of 705 streaks in these images, of which 49 were analyzed in detail. The distance between WISPR and the debris particles inferred from the streak widths is estimated to be between 1 m and 6 m. Streak brightness values were typically less than 20 pMSB, and the streak lengths varied from less than 100 pixels to the full FOV.

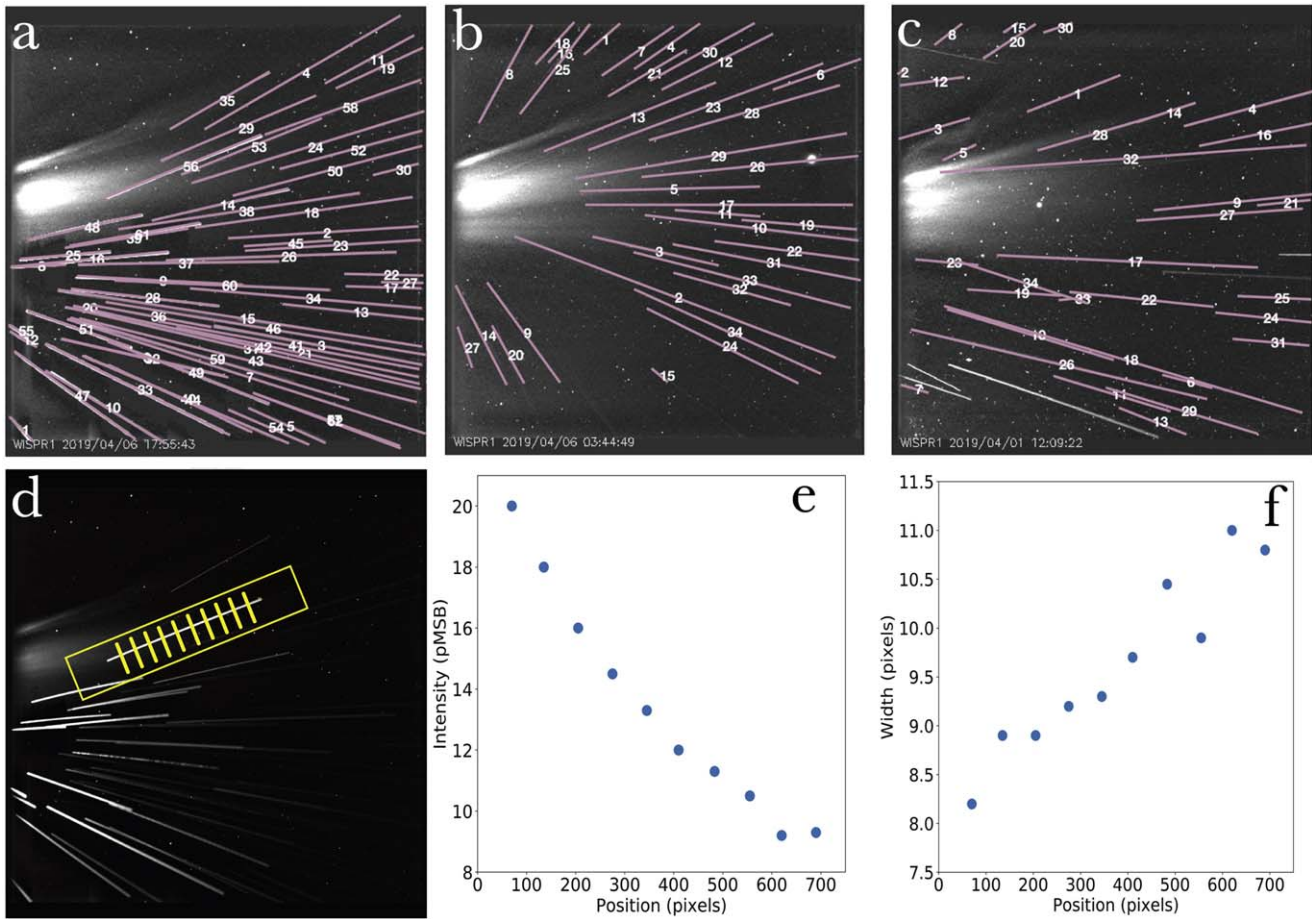
Figures 8(a)–(c) show three examples of images that were analyzed. The image in Figure 8(a) started integration at 2019-04-06/17:55:43 UTC. This image has  $QF = 7$ , and 62 unique streaks are identified and labeled. The image in Figure 8(b) started integration at 2019-04-06/03:44:50 UTC. This image has  $QF = 5$ , and 34 unique streaks are identified and labeled. The image in Figure 8(c) started integration at 2019-04-01/12:09:22 UTC. This image was assigned  $QF = 4$ , and 34 unique streaks are identified and labeled.

Figure 8(d) contains the same image data as Figure 8(a), but has a single streak (#56) highlighted to demonstrate the streak analysis procedure. Summing the measured intensities along a streak provides the total energy input into the detector as the

fragment passed across the imager FOV. Figure 8(e) shows the measured intensity at the image locations of the 10 tick marks indicated in Figure 8(d), in units of pMSB. Figure 8(e) shows the measured streak width at the same 10 image locations. Converting the measured detector energy into incident power (using the WISPR conversion factor described above) allows the fragment passage time to be determined. By assuming a fragment velocity, the time in the FOV can be found and multiplied by the detector power to produce the estimated counts measured by the detector. The fragment velocity and size are adjusted until the estimated detector counts match the measured value.

Results of this analysis suggest that the fragments producing the WISPR image streaks are moving at speeds of a few meters per second relative to the WISPR FOV. Measured streak lengths support the conclusion that the streaks are made by slowly moving fragments. Each WISPR image is a collection of exposures (Section 2). Any fragment moving at more than a few meters per second would cross the entire image during a single exposure. For nearly all of the images and streaks analyzed, the drifting fragments appear to be moving at a few meters per second or less.

Once the fragment velocity has been bounded, fragment size can be inferred. The scattered/reflected light hitting the detector is measured by the streak intensity. The intensity is related to both the fragment size and speed, as shown in Figure 9 for streaks 56 and 47 from the WISPR image in Figure 8(a). A faster fragment must deposit more photons per unit time, implying a larger diameter, to produce the same total energy deposition as a slower fragment. A significant uncertainty in this relationship is the scattering efficiency of the fragment. For simplicity, we assume a spherical perfectly reflecting fragment. Within the range of scattering phase angles valid for the WISPR-I FOV (Figure 9(a)), the scattering function varies sharply, dropping by orders of magnitude from the boresight direction to the outer boundary of the FOV. This effect dominates the light entering the detector as the fragment moves across the FOV for WISPR-I images, often making it difficult to see expected intensity changes as the fragment distance changes. A smoother variation of intensity along the streaks imaged with the outer camera is observed, consistent



**Figure 8.** (a), (b), and (c): WISPR images with distinct streaks, where each streak has been assigned an identifying number (see the text for detail). (d) Data from (a), with streak #56 highlighted. (e) Streak intensity at each of the 10 tick mark locations indicated in (d), from left to right. (f) Streak width at each of the 10 tick mark locations indicated in (d), from left to right.

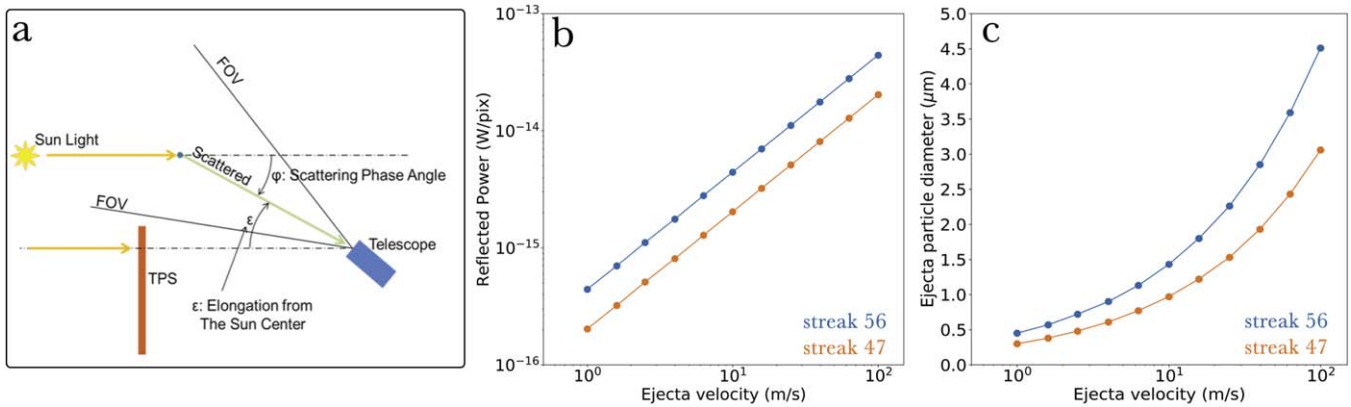


**Figure 9.** (a) Geometry of scattered/reflected light entering the WISPR aperture, considering the FOV, PSP Thermal Protection System (TPS) heat shield, and the scattering phase angle. (b) Predicted total reflected power that enters WISPR as a function of debris particle velocity. (c) Estimated debris particle diameter as a function of debris particle velocity.

with expected variation at large phase angles. Figure 9(c) shows the estimated relationship between fragment diameter and velocity for streaks 56 and 47 from the WISPR image in Figure 8(a) over the range of velocities inferred from the streak analysis. Drift velocities of  $<10 \text{ m s}^{-1}$  relative to the spacecraft imply debris fragment diameters on the order of  $1 \mu\text{m}$ .

Assuming identical spherical debris fragments with  $1 \mu\text{m}$  diameter with a density between kapton ( $\sim 1400 \text{ kg/m}^{-3}$ ) and aluminum ( $\sim 2710 \text{ kg/m}^{-3}$ ), the 62 streaks in Figure 8(a)

correspond to  $\sim 46$  to  $\sim 88 \text{ pg}$  of liberated debris material in the WISPR FOV. By comparison, a sphere of olivine with  $88 \text{ pg}$  mass would have a radius of  $\sim 2 \mu\text{m}$ . Events like Figure 1(e) show hundreds of streaks, and a substantial amount of ejected material is likely smaller than WISPR can detect (Section 4.2), implying that the total liberated debris material per impact can be one or two orders of magnitude larger than the values estimated here. These estimates are order-of-magnitude calculations assuming that streak #56 from the WISPR image in

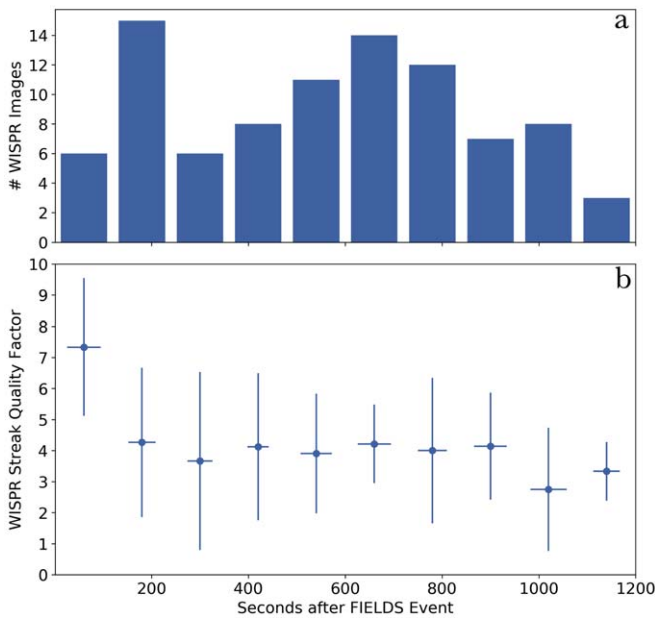


**Figure 10.** (a) Number of WISPR images in each 120 s time bin. (b) Average WISPR streak quality flag as a function of time between the start of a FIELDS long-duration spacecraft potential perturbation event and the start of a WISPR image capture. Error bars represent one standard deviation in quality flag value and delay time.

Figure 8(a) yields representative debris fragment properties. A more accurate analysis requires statistically significant distributions of debris fragment properties and careful uncertainty estimation, which are beyond the scope of the current work.

Using a shock-physics-based computation (Iyer et al. 2013, 2015a), a  $5\ \mu\text{m}$  diameter dust grain impacting the PSP aluminum radiator at  $20\ \text{km s}^{-1}$  with normal incidence was evaluated. At this impact speed, the ejecta is expected to comprise vapor, melt droplets, and solid fragments. This diameter represents the lower end of dust grains expected to be gravitationally bound to the Sun. Dust grains two or four times smaller are expected to become  $\beta$ -meteoroids (Szalay et al. 2020). The impact-produced molten droplets are predicted to be submicron in size. These (and the vapor) will be too small (sparse) for WISPR’s imaging capability. Solid fragments are predicted with  $1.5\text{--}15\ \mu\text{m}$  diameter with an average fragment diameter of  $5\ \mu\text{m}$ , and velocities relative to the spacecraft of  $1\text{--}600\ \text{m s}^{-1}$ . The number of solid fragments ejected is predicted to be less than  $\sim 200$ . The predicted cone angle of the ejecta cloud ranges from near-zero to  $30^\circ$ . The fragment properties (diameter, velocity, number of large fragments) determined from the WISPR data analysis presented here are consistent with the low end of the predicted fragment properties.

### 3.7. Correlations between FIELDS and WISPR Debris-cloud Detection

Figure 1 shows an individual event where FIELDS and WISPR detect the same debris cloud. Here, the 240 identified FIELDS long-duration potential perturbation events and the WISPR image QF database are compared to evaluate the correlation between FIELDS and WISPR signatures of debris clouds. The database includes 5521 images from WISPR-I and 3283 from WISPR-O.

First, all WISPR images recorded  $<1200\ \text{s}$  after a FIELDS long-duration potential perturbation event are identified. A time delay is calculated between the start of a FIELDS long-duration spacecraft potential perturbation event and the start of a WISPR image capture. The events are then organized into 120 s bins, and the average WISPR streak QF determined for each bin. Figure 10(a) shows the number of WISPR images in each bin, and Figure 10(b) shows the average QF in each time bin. Vertical error bars correspond to one standard deviation of the QF values in that bin, and horizontal error bars correspond to one standard deviation of the delay times for events in that bin.

Significant variation from the overall trend is expected because FIELDS is sensitive to impacts anywhere on the spacecraft, while WISPR is sensitive only within a finite FOV. This consideration, combined with the low statistics per bin, result in wide vertical error bars. Still, an overall trend is evident in that images where the integration time begins further after the initial impact have fewer streaks, and images where the integration time begins closer to the dust impact have more streaks. This behavior is consistent with the interpretation developed thus far that the FIELDS long-duration potential perturbation events are signatures of debris-producing dust impacts.

### 3.8. Correspondence with Star Tracker Demotions

During the first eight orbits of PSP, there were 12 unique star tracker anomalous demotions: times when the star trackers had to be reset because they could not achieve an attitude solution due to environmental conditions. All demotions were recovered from after a few minutes.

The PSP star trackers process data at 10 Hz, and communicate with the spacecraft at 1 Hz. For the star tracker demotions observed near dust-impact events, the star tracker does not report a hardware problem, but also does not provide an attitude solution. This causes the spacecraft to demote the star tracker operational mode. The reported star tracker demotion times reported here are expected to lag the initial dust-impact event by the time it takes for debris to clear the FOV (up to a few minutes), plus the time it takes to acquire a new attitude solution (a few seconds), plus the time required for the spacecraft to promote the star tracker back to its normal operational mode ( $\sim 10\ \text{s}$ ).

Figure 11 lists all demotion events. It also indicates the closest preceding FIELDS microsecond dust-impact spike, indicative of a dust-impact-plasma cloud, and the closest preceding FIELDS long-duration spacecraft potential perturbation event, indicative of a debris cloud. The starting integration time of the closest WISPR image with streaking is indicated, as is the WISPR QF. Table cells are marked with “Insufficient Data” when the data required to evaluate any of these criteria do not exist within 24 hr of the demotion. FIELDS or WISPR events that occur close in time to star tracker demotions are indicated in blue.

The data in Figure 11 demonstrate a connection between long-duration spacecraft potential perturbation events like the one shown in Figure 1, WISPR image streaking, and star tracker demotions. Long-duration spacecraft potential perturbation events (240) and star tracker demotions (12) are rare within the PSP data set, making the probability exceedingly low (unless they were correlated) that, of the 11 star tracker demotions with appropriate FIELDS data to observe such effects, eight occurred less than a few minutes after long-

Demotion ID	ST demotion event (mm/dd/yyyy UTC)	Sun distance ( $R_S$ )	Preceding FIELDS $\mu$ s spike	$\Delta t$ (s) to demotion	Preceding long-duration FIELDS signature	$\Delta t$ (s) to demotion	Closest WISPR streaked image integration start time	$\Delta t$ (s) from demotion	WISPR QF
ST1-308	11/04/2018 00:11:40	39.13	11/04/2018 00:10:30	70	11/04/2018 00:10:30	70	11/04/2018 00:00:50	-650	2
ST2-309	11/05/2018 00:35:04	36.77	11/05/2018 00:33:20	104	11/05/2018 00:33:20	104	11/05/2018 00:33:28	96	9
ST1-309	11/05/2018 00:39:55	36.77	11/05/2018 00:33:20	395	11/05/2018 00:33:20	395	11/05/2018 00:33:28	387	9
ST1-031	01/31/2020 14:46:55	33.54	01/31/2020 14:45:50	65	01/31/2020 14:45:50	65	01/31/2020 14:46:19	-36	9
ST2-163	06/11/2020 04:23:50	42.36	06/11/2020 04:23:20	30	06/09/2020 13:10:30	141,200	06/11/2020 04:00:19	-1,411	6
ST1-243	08/30/2020 11:25:44	143.84	08/30/2020 11:08:20	1044	08/27/2020 04:07:30	285,494	Insufficient data	-	-
ST1-268	09/24/2020 10:51:30	35.69	09/24/2020 10:50:10	80	09/24/2020 10:47:30	240	09/24/2020 10:30:25	-1,265	3
ST1-320	11/15/2020 09:43:47	173.72	11/15/2020 09:12:10	1897	Insufficient data	-	Insufficient data	-	-
ST1-020	01/20/2021 05:27:23	32.04	01/20/2021 05:26:30	53	01/20/2021 05:26:30	53	01/20/2021 05:05:34	-1,309	2
ST2-020	01/20/2021 05:27:23	32.04	01/20/2021 05:26:30	53	01/20/2021 05:26:30	53	01/20/2021 05:05:34	-1,309	2
ST1-112	04/22/2021 05:29:21	65.58	04/22/2021 05:28:40	41	01/22/2021 02:36:00	10,401	Insufficient data	-	-
ST2-120	04/30/2021 01:44:00	18.06	04/30/2021 01:42:05	115	04/30/2021 01:42:05	115	Insufficient data	-	-

**Figure 11.** List of star tracker demotion events during PSP’s first eight solar encounters. The affected star tracker (1 or 2) is indicated in the first column. Times of preceding FIELDS microsecond dust-impact spikes and FIELDS long-duration spacecraft potential perturbation events, and WISPR streaked images are indicated, as well as time delay  $\Delta t$  between these signatures and each demotion.

duration spacecraft potential perturbation events. Of the 12 star tracker demotions, 10 showed a short-duration FIELDS signature indicative of a dust-impact-plasma cloud within a few minutes prior to the demotion. This second observation is weaker evidence of a correlation between impacts and demotions, because the count rate for dust-impact-plasma-cloud potential perturbations significantly exceeds one per minute during portions of the PSP orbit (Malaspina et al. 2020a).

For each of the three times when a WISPR image was recorded within a few minutes of a star tracker demotion, the image QF was 9, indicating an event where the image is dominated by streaks.

Not all star tracker demotion events show a corresponding impact-plasma spike, FIELDS debris-cloud, or WISPR debris-cloud signature, emphasizing how strongly the impact location determines the ability of FIELDS and WISPR to detect impact debris. The primary FIELDS antenna are mounted in the plane of the heat shield, while the WISPR imaging FOV is toward the spacecraft +x and +z directions (along the spacecraft direction of motion at perihelion and toward the Sun, respectively), and the star tracker imaging FOVs are toward the spacecraft  $-z$  direction (anti-sunward). Therefore all three of the detectors sensitive to debris clouds cover different portions of the spacecraft. Only impact events producing dense debris clouds that envelop the entire spacecraft are expected to be detected by FIELDS, WISPR, and the star trackers at once (such as the event in Figure 1). For less extreme debris events, impact location is expected to strongly determine the degree to which FIELDS or WISPR can detect debris-cloud signals.

The star tracker demotions, when telemetry was collected during these anomalies, all show lost tracking due to insufficient valid stars and noisy star fields at various levels. There were no signs of internal anomalies occurring during the reset periods, indicating that the demotions were environmentally related. Potential environmental causes are a large number of reflective particles in the star tracker FOV or a proton impact event. Since in most cases only one star tracker was affected, proton impact is not a likely cause.

## 4. Discussion

### 4.1. Impactor Mass Estimate

The plasma waves observed during the debris-producing impact event shown in Figure 5 can be combined with the

current understanding of impact-plasma charge yield to estimate the mass and radius of the impactor.

At the time of the impact shown in Figure 5, PSP was  $51.8 R_S$  ( $\sim 0.24$  au) from the Sun. Assuming that the impactor is a dust grain on a nearly circular orbit, this corresponds to an expected impact velocity of  $\sim 25$  km  $s^{-1}$  (Szalay et al. 2020, Figure 2). Based on laboratory studies of impact charge yield on PSP heat shield samples, the plasma charge yield for a hypervelocity impact is  $Q_{\text{impact}} = 0.043 m_{\text{dust}} v_{\text{impact}}^{3.46}$  (for  $m_{\text{dust}}$  in kilograms and  $v_{\text{impact}}$  in kilometers per second; Shen 2021). Dividing the total impact-produced charge by the charge on a proton yields the total number of ions in the plasma cloud, assuming that most are singly ionized. If the ions in the cloud are distributed uniformly through a volume  $V_{\text{cloud}}$ , then cloud ion density can be written as,

$$n_{\text{cloud}} = \frac{Q_{\text{impact}}}{q_p V_{\text{cloud}}}. \quad (1)$$

Based on laboratory studies, the impact-plasma cloud can be approximated as a spherical cone (Shen et al. 2021a). If we assume a half-open angle of  $\theta = 20^\circ$ , the volume becomes,

$$V_{\text{cloud}} = \frac{2\pi}{3} r_{\text{cloud}}^3 (1 - \cos(\theta)) \quad (2)$$

where  $r_{\text{cloud}} \approx v_{\text{expansion}} \Delta t$ . Solving for  $m_{\text{dust}}$ :

$$m_{\text{dust}} = \frac{q_p n_{\text{cloud}} V_{\text{cloud}}}{0.043 v_{\text{impact}}^{3.46}}. \quad (3)$$

These equations should enable one to estimate the mass of the impacting dust grain if the density of the plasma cloud is known at a given cloud radius.

The Langmuir waves in Figure 5 indicate that the cloud density reaches the ambient plasma density  $\Delta t = 0.1535$  s after impact. Assuming a constant cloud expansion speed of  $10$  km  $s^{-1}$  (see Section 3), and the equations above, one arrives at a dust grain mass of  $5.9 \times 10^{-5}$  kg. Given the density of olivine  $\sim 3500$  kg  $m^{-3}$ , this corresponds to a spherical dust grain with a  $1.6$  mm radius. Such a particle is massive enough to catastrophically damage the spacecraft if it were to puncture a radiator water tube (Iyer et al. 2015a). From the analysis in Section 3, PSP has weathered hundreds of such debris-producing impacts without catastrophic damage, suggesting that the dust mass is significantly over-estimated using the above assumptions.

In the prior calculation, it was assumed that the impact plasma was uniformly distributed throughout the volume of an expanding spherical cone. However, the impact plasma is created over a much shorter time than the expansion time of the plasma plume. Therefore, it is more physical to assume that the impact plasma is confined to a volume at the forward expanding edge of that cone. In this case, the plasma will occupy a volume of

$$V_{\text{cloud}} = \frac{2\pi}{3}(r_{\text{outer}} - r_{\text{inner}})^3(1 - \cos(\theta)), \quad (4)$$

for an outer cloud radius defined as  $r_{\text{outer}} \approx v_{\text{expansion}}\Delta t$ . For the leading edge plasma to generate coherent Langmuir waves, it must have a spatial extent on the order of at least a few Debye lengths  $\lambda_D$ . Given the ambient plasma conditions at the time of impact ( $n_e = 142.8 \text{ cm}^{-3}$ ,  $T_e = 22 \text{ eV}$ ),  $\lambda_D \approx 2.7 \text{ m}$ . Using  $r_{\text{inner}} = r_{\text{outer}} - 5\lambda_D$  and the above equations, with Equation (4) instead of Equation (2), the estimated impactor mass becomes  $5.0 \times 10^{-11} \text{ kg}$ , which corresponds to a spherical olivine dust grain with a  $15.1 \mu\text{m}$  radius. An impactor of this radius is large enough to be an interplanetary dust grain on a near-circular gravitationally bound orbit (Szalay et al. 2020), consistent with the radial occurrence rates in Figure 6, yet also small enough to be consistent with the observation that PSP has encountered hundreds of such impacts without catastrophic damage.

For this plasma-cloud model, where the impact plasma is confined to the forward edge of an expanding spherical cone, the estimated impactor radius increases linearly with increasing  $r_{\text{inner}}$ , increases nearly linearly with decreasing  $v_{\text{impact}}$ , depends very weakly on  $\theta$ , and is entirely insensitive to  $v_{\text{expansion}}$  or  $\Delta t$ . These last dependencies occur because  $r_{\text{outer}}$  drops out of the calculation for plasma-cloud volume under the assumptions made in this model.

#### 4.2. Long-duration Electric Potential Perturbation Hypothesis

Similar long-duration electric potential perturbations associated with debris clouds to those reported here were previously reported in association with dust impacts on the Magnetospheric MultiScale mission (MMS) spacecraft (Williams et al. 2016; Vaverka et al. 2018). However, the physical mechanism by which potential perturbations last tens of seconds to over a minute has not yet been established. Based on the considerations elaborated on below, we hypothesize that the perturbation is due to induced charging of the FIELDS antennas by a slowly expanding cloud of charged debris fragments.

Processes related to impact ionization and the plasma it produces are expected to exhaust themselves on much faster timescales than tens of seconds. Plasma clouds are expected to expand with initial velocities on the order of  $10 \text{ km s}^{-1}$  (Lee et al. 2012), and so expand past the  $\sim 2 \text{ m}$  antennas in a few hundred microseconds. Discharge of collected impact-plasma charge to the ambient thermal plasma by spacecraft surfaces after impact-liberated plasma collection is predicted to follow  $\tau = 0.5(C_{\text{sc}}T_{\text{ph}})/(\epsilon_0 n_e v_{\text{the}} A_{\text{sc}})$  (Zaslavsky 2015; O’Shea et al. 2017). For a quantitative estimate, the discharge time of one antenna is considered (length =  $2 \text{ m}$ , diameter =  $3.175 \text{ mm}$ ), because the lower free-space capacitance of an antenna compared to the spacecraft body should result in a slower discharge time. In this equation, the free-space capacitance of the antenna is  $C_{\text{ant}}$ , photoelectron temperature is  $T_{\text{ph}}$ , ambient plasma density and electron thermal velocity are  $n_e$  and  $v_{\text{the}}$ ,

respectively, and the full surface area of the antenna is  $A_{\text{ant}}$ . For the event in Figure 1:  $T_{\text{ph}} \approx 2 \text{ eV}$ ,  $n_e \approx 410 \text{ cm}^{-3}$ ,  $T_e \approx 34 \text{ eV}$ ,  $C_{\text{ant}} \approx 18 \text{ pF}$ , and  $A_{\text{ant}} \approx 0.02 \text{ m}^2$ . With these parameters, a discharge time constant on the order of  $20 \mu\text{s}$  is predicted. The observations in Section 3 show that the initial dust-impact voltage perturbation lasts for  $1 \text{ ms}$ , ion cloud initial expansion speeds (from the SCM perturbation timing) are consistent with  $10 \text{ km s}^{-1}$ , interruption of natural plasma waves lasts for  $\sim 0.35 \text{ s}$ , and driven plasma wave activity lasts for  $\sim 0.3 \text{ s}$ . All of these predicted and observed impact-plasma timescales are much shorter than the tens of seconds over which the long-duration electric potential perturbations are observed. Given this information, we hypothesize that the long-duration perturbations are driven by an interaction between spacecraft surfaces and a (relatively) slowly expanding charged debris cloud.

As spacecraft debris fragments expand outward, they will encounter the ambient solar wind thermal plasma, as well as photon flux from the Sun. As a result, they will experience surface charging, quickly reaching a surface potential that causes the net current to and from their surface to be zero, similar to any spacecraft surface (e.g., Garrett 1981) or natural dust grain (e.g., Mann et al. 2014 and references therein). The presence of curved streaks in WISPR images (see the Appendix) is also qualitatively consistent with the idea that the debris-cloud fragments are charged and can interact electrostatically with the spacecraft.

Given the ambient thermal plasma density and temperature ( $\sim 410 \text{ cm}^{-3}$ ,  $34 \text{ eV}$ ) and solar distance ( $r_{\text{psp}} = 36.7 R_S$ ) for the event in Figure 1, the surface potential ( $V_s$ ) on a  $1 \mu\text{m}$  diameter sphere (Section 3.6) can be estimated by assuming a net zero current to and from the sphere,

$$I_{\text{total}} = I_{\text{photo}} + I_{\text{the}} + I_{\text{thi}}. \quad (5)$$

The photoelectron current ( $I_{\text{photo}}$ ), electron thermal current ( $I_{\text{the}}$ ), and ion thermal current ( $I_{\text{thi}}$ ) are defined in the standard ways (e.g., Garrett 1981),

$$(V_s \leq 0) \quad I_{\text{photo}} = A_{\text{cs}} J_{\text{photo0}} \quad (6)$$

$$(V_s > 0) \quad I_{\text{photo}} = A_{\text{cs}} J_{\text{photo0}} ((1 - \alpha)e^{-V_s/v_1} + \alpha e^{-V_s/v_2}) \quad (7)$$

$$(V_s \leq 0) \quad I_{\text{the}} = A_{\text{full}} J_{\text{the0}} \left( 1 + \frac{qV_s}{k_B T_e} \right) \quad (8)$$

$$(V_s > 0) \quad I_{\text{the}} = A_{\text{full}} J_{\text{the0}} (e^{qV_s/k_B T_e}) \quad (9)$$

$$(V_s \leq 0) \quad I_{\text{thi}} = A_{\text{full}} J_{\text{thi0}} \left( 1 - \frac{qV_s}{k_B T_i} \right) \quad (10)$$

$$(V_s > 0) \quad I_{\text{thi}} = A_{\text{full}} J_{\text{thi0}} (e^{-qV_s/k_B T_i}) \quad (11)$$

where the sphere full surface area is  $A_{\text{full}}$ , the cross-sectional area is  $A_{\text{cs}}$ ,  $\alpha = 0.05$ ,  $v_1 = 2.7V$ , and  $v_2 = 10V$  (Ergun et al. 2010).  $T_e$  and  $T_i$  are the electron and ion temperatures in units of kelvin, and  $k_B$  is Boltzman’s constant. The absolute value of the charge on an electron is represented by  $q$ , allowing the signs associated with particle charge to be explicitly included in these equations. The thermal electron flux is  $J_{\text{the0}} = qn_e v_{\text{the}}$  for electron density  $n_e$  and electron thermal velocity  $v_{\text{the}} = \sqrt{2k_B T_e/m_e}$  for electron mass  $m_e$ . The ion thermal flux is defined similarly, using ion temperature, density, and mass in place of the electron quantities. For photoelectron current yield,

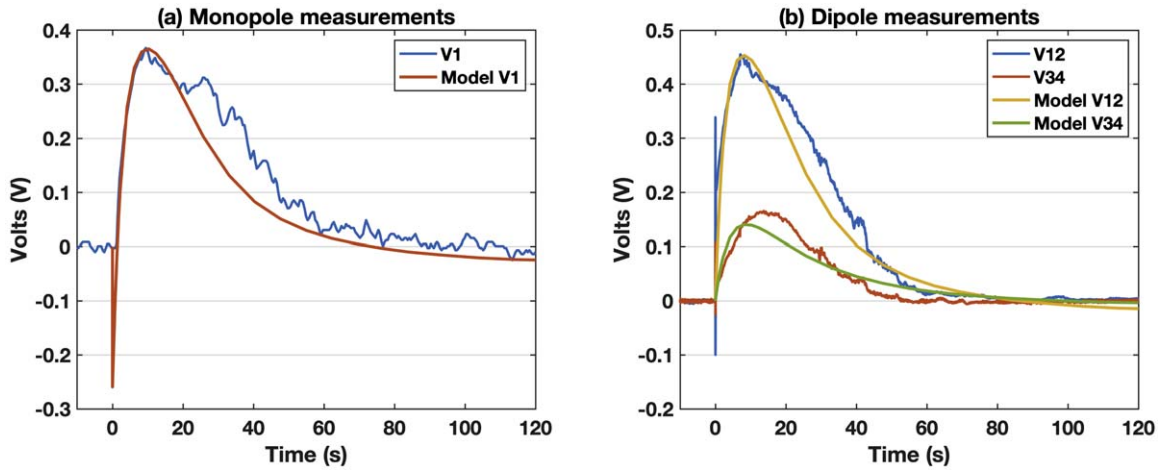


**Figure 12.** Measured monopole (a) and dipole (b) responses to the electric potential of the expanding debris cloud. These data are also shown in Figures 1(a) and (b). Model best-fit values for monopole (a) and dipole (b) signals are shown as smooth lines. See the text for details.

we use  $J_{\text{photo0}} = (40 \mu\text{A}/\text{m}^2)(r_{1\text{ AU}}/r_{\text{psp}})^2$ , a reasonable value for conducting spacecraft materials (Diaz-Aguado et al. 2019).

Solving these equations for the stated conditions yields a surface potential on a  $1 \mu\text{m}$  diameter debris fragment sphere of  $+1.14 \text{ V}$  relative to infinity. The time required to charge a debris fragment can be estimated using the definition of current  $I = \Delta Q/\Delta t$ . The  $\Delta Q$  acquired by the fragment is  $C\Delta V$ , where  $C = 4\pi\epsilon_0 r_{\text{sphere}}$  and  $\Delta V = 1.14 \text{ V}$ , and the total current can be approximated as  $I_{\text{photo}} = A_{\text{cs}} J_{\text{photo0}}$ . Using all parameters defined thus far,  $\Delta Q \approx 6.3 \times 10^{-17} \text{ C}$ ,  $I \approx 1.08 \times 10^{-15} \text{ A}$ , and therefore  $\Delta t \approx 0.059 \text{ s}$ . Therefore, the debris fragments are expected to charge rapidly compared to the  $\sim 0.2 \text{ s}$  required for them to travel  $2 \text{ m}$  from the impact location with a cloud expansion velocity of  $10 \text{ m s}^{-1}$  (see Section 3.6).

As a positively charged cloud expands away from the impact location, it will induce a positive potential on the spacecraft and antennas (Shen et al. 2021a). Production of voltage perturbations due to induced charging of electric field antennas by expanding charge clouds following hypervelocity impacts has recently been demonstrated in laboratory experiments (Shen et al. 2021a). We propose that the charged cloud of debris fragments produces voltage perturbations on the FIELDS antennas by the same mechanism. This mechanism is not limited to thermal plasma discharge timescales because induced charging is a rearrangement of existing charge on a conductor (the antennas) due to the electric field associated with the electric potential of the debris cloud. It does not add or subtract net charge from the antenna. In this way, voltage perturbation from induced charging resembles the detection of an electric field by an antenna.

With this mechanism, the time-extent of a detected long-duration potential perturbation signal is determined by the charge density and expansion rate of the debris cloud. The relative response of each FIELDS antenna will depend on the proximity of the cloud to each antenna, just as in laboratory experiments (Shen et al. 2021a). Further, the response of the spacecraft body should be much reduced compared to that of the antennas for most events. This is because the debris cloud will generally expand perpendicular to the spacecraft body surface regardless of impact location, but a debris cloud created by an impact on the spacecraft body near the heat shield can travel parallel to one or more of the FIELDS antennas for an extended duration.

To demonstrate the feasibility of this mechanism, the antenna charging model of Shen et al. (2021a) is applied to fit the data in Figure 1. For this comparison, a 7:1 scaled-up version of the spherical model utilized in laboratory experiments and numerical simulation by Shen et al. (2021a) is used. This model treats the PSP spacecraft bus as a  $1 \text{ m}$  sphere with four orthogonally mounted  $2 \text{ m}$  antennas extending from it. Considered impact locations are  $10^\circ$ ,  $30^\circ$ , and  $45^\circ$  between any two antennas (e.g.,  $10^\circ$  away from antenna  $V_2$  toward antenna  $V_4$ ). The expanding debris cloud is treated as a point charge in the plane of the four antennas. Discharge of impact-plasma charges collected by the antennas and spacecraft to the ambient environment via thermal plasma is included. A Maxwell capacitance matrix is employed to model the capacitive coupling between the elements of the system (i.e., PSP spacecraft and FIELDS antennas) and is used to calculate the measured voltages developed on them. The spacecraft, antennas, and stray capacitance values are taken to be  $200 \text{ pF}$ ,  $18 \text{ pF}$ , and  $36 \text{ pF}$ , respectively (Pulupa et al. 2017; Diaz-Aguado et al. 2021). The following model parameters are allowed to vary until a best fit is found between the model solution and the data: debris-cloud radial expansion velocity, debris cloud total charge, and impact location. Both monopole and dipole data are fit simultaneously, with equal weighting, to determine the best-fit solution.

The best-fit solution is shown in Figure 12(a), for monopole data, and Figure 12(b), for dipole data. This solution has an impact location  $30^\circ$  away from antenna  $V_1$  toward antenna  $V_3$ . This solution has a debris-cloud total charge of  $1.93 \times 10^{-10} \text{ C}$  and a cloud radial expansion speed of  $\sim 8 \text{ cm s}^{-1}$ .

The model fit velocity is significantly lower than the few-meters-per-second debris fragment velocity estimated using WISPR data in Figure 9(c). However, there are a few possible reasons why this may not be a strong contradiction. First, the induced charge model fitting provides the radial group speed of the debris cloud away from the spacecraft in the plane of the four antennas. This direction is nearly perpendicular to the direction along which debris fragments must move to create well-defined streaks in WISPR. Therefore it is possible that the two debris-cloud expansion estimates measure nearly orthogonal components of the cloud velocity. Second, the event in Figure 1 is one of the longest-duration debris-cloud potential

perturbation signatures observed by PSP, lasting over a minute. Most events are between 1 and 20 s (e.g., Figures 3, 5), suggesting that the event in Figure 1 had a slower debris-cloud expansion than most events.

Liberation of slowly expanding debris may occur if an impact sufficiently weakens a section of brittle spacecraft surface material larger than the immediate impact site, or if the impact exposes an underlying region of less tightly bound material. Both of these situations may be applicable to the heat shield, and both may result in a debris-cloud expanding more slowly ( $\sim 8 \text{ cm s}^{-1}$  radially away from the spacecraft–Sun axis) compared to the debris expansion velocities ( $\sim 1 \text{ m s}^{-1}$ ) inferred from streak analysis of other events with fewer debris streaks (Section 3.6). Slow debris expansion could also explain times as long as 6.5 minutes between FIELDS dust-impact observations and star tracker demotions (Figure 11).

The model fit debris-cloud total charge ( $1.93 \times 10^{-10} \text{ C}$ ) is significantly larger than the surface charge carried by one  $1 \mu\text{m}$  diameter debris fragment ( $6.3 \times 10^{-17} \text{ C}$ ), or even hundreds of such fragments (Section 3.6). However, there is strong evidence from laboratory and theoretical work that high-velocity impacts produce many more fine particles than large particles (e.g., Trucano et al. 1989; Zhou et al. 2006; Nishida et al. 2012). Further, laboratory studies show that as the kinetic energy of a hypervelocity impact increases, the ejecta size distribution follows a steeper power law (McDermott et al. 2016). In other words, a larger fraction of the ejecta from impacts with high kinetic energy is made up of finer fragments. Given this behavior of high-velocity impact ejecta, the total charge carried by the debris-cloud material should be distributed over a range of fragment sizes. To estimate the total electric charge carried by the debris cloud, we assume that the debris fragments follow a collisional fragmentation power-law size distribution with a differential power index of  $\mu$  (Langevin & Arnold 1977), and we assume that WISPR detects only the largest fragments from this distribution,  $> 0.5 \mu\text{ m}$ . The total number of particles  $N_{\text{tot}}$  can then be calculated as  $N_{\text{tot}} = \int n_0 \cdot a^\mu da$ , where  $a$  is the radius of (assumed spherical) particles, and  $n_0$  is a normalization constant. Solving for  $n_0$ :  $n_0(\mu) = N_{\text{tot}}(a_{W \text{ max}}^{\mu+1} - a_{W \text{ min}}^{\mu+1})/(\mu + 1)$ , where  $N_{\text{tot}} = 200$  is the assumed number of fragments with radii between  $a_{W \text{ max}} = 2 \mu\text{m}$  and  $a_{W \text{ min}} = 0.5 \mu\text{m}$ . These values are consistent, to order of magnitude, with the streak analysis in Section 3.6. Debris particles experience similar surface charging processes as the spacecraft. Under the ambient plasma conditions and charging equations described above, debris fragments are estimated to reach an equilibrium potential of  $\phi_{db} = +1 \text{ V}$  within a fraction of a second.

The total amount of electric charge carried by the debris particles ( $Q_{db}$ ) can therefore be written as  $Q_{db} = \int_{a_{\text{min}}}^{a_{\text{max}}} (4\pi\epsilon_0 \phi_{db} a) \cdot n_0(\mu) a^\mu da = (4\pi\epsilon_0 \phi_{db} n_0(\mu)) \cdot \int_{a_{\text{min}}}^{a_{\text{max}}} a^{1+\mu} da$ , where  $\epsilon_0$  is the vacuum permittivity.  $a_{\text{min}}$  and  $a_{\text{max}}$  are the minimum and maximum, respectively, radii for fragments in the debris cloud. If we assume  $a_{\text{max}} = 2 \mu\text{m}$  and  $a_{\text{min}} = 20 \text{ nm}$ , and  $\mu = -3.1$  (consistent with fragmentation of freshly broken rock (Langevin & Arnold 1977) or fragmentation of brittle metals during high-velocity ( $> 2 \text{ km s}^{-1}$ ) impacts (Hooper 2012)), then  $Q_{db}$  is found to be  $\sim 7.7 \cdot 10^{-13} \text{ C}$ . This value is still  $\sim 150$  times smaller than the model-estimated charge carried by the debris cloud.

However, the integral for  $Q_{db}$  depends strongly on  $\mu$ , and current laboratory capabilities cannot reproduce the

combination of impactor mass and impact velocity experienced by PSP. McDermott et al. (2016) reported that fragment size distributions from hypervelocity impacts ( $3 \text{ km s}^{-1}$  to  $6 \text{ km s}^{-1}$ ) yield a steeper power-law index as the impact velocity increases. Using  $\mu = -4.9$  (consistent with a higher production of finer particles; Langevin & Arnold 1977) produces a  $Q_{db}$  of  $1.7 \cdot 10^{-10} \text{ C}$ , which is reasonably consistent with the model fit given the back-of-the-envelope estimate used here. In addition, one can decrease  $a_{\text{min}}$  to achieve more charge. Decreasing  $a_{\text{min}}$  to  $10 \text{ nm}$  increases  $Q_{db}$  by a factor of two for the case of  $\mu = -3.1$  and by a factor of seven for the case of  $\mu = -4.9$ . There will be a lower bound to  $a_{\text{min}}$  (in the range of tens of nanometers) below which debris-cloud particles have charge-to-mass ratios that cause them to be swept away by the solar wind motional electric field on timescales significantly less than 1 minute. These smallest particles will therefore not contribute to the portion of the debris cloud whose surface charging creates the observed long-duration potential perturbations.

Given the sensitivity of  $Q_{db}$  estimates to the collisional fragmentation power-law index and the lower-bound fragment radius, both of which are poorly constrained for PSP impacts, this analysis is limited to demonstrating that the induced-charging hypothesis is potentially feasible. Additional study beyond the scope of this work is required to test this hypothesis more robustly.

## 5. Conclusions

PSP experienced a large number of hypervelocity dust impacts during its first eight orbits through the densest part of the zodiacal cloud. A number of phenomena are generated by these impacts, including short- and long-duration perturbations to the electric potential near the spacecraft, streaks in the WISPR images, magnetic field perturbations near the spacecraft, plasma waves driven by impact plasma, and star tracker attitude solution loss. The observations and analysis presented here demonstrate the properties, occurrence, and connections between these phenomena.

A comprehensive picture emerges from this analysis. Relatively large ( $> 10 \mu\text{m}$ ) gravitationally bound interplanetary dust grains strike the spacecraft. Dense plasma clouds are generated that can perturb the electric and magnetic fields local to the spacecraft on  $< 1 \text{ ms}$  timescales. These plasma clouds can be dense enough to (i) create magnetic pressure pulses at the ion cloud expansion front, (ii) drive plasma waves as they are accelerated (picked up) to solar wind velocities, and (iii) temporarily prevent natural plasma waves from reaching the spacecraft. These plasma effects occur on  $< 1 \text{ s}$  timescales. Some impacts liberate clouds of spacecraft material (debris). The debris passes through imager FOVs, creating streaks in WISPR, and creating temporary star tracker attitude solution loss. The debris fragments undergo surface charging in the ambient solar wind environment and can produce long-duration ( $< 1 \text{ minute}$ ) perturbations to the electric potential near the spacecraft. These perturbations cease when the debris cloud disperses from expansion and/or debris-cloud particles are removed by solar wind electromagnetic acceleration. Debris clouds are sufficiently diluted to cease dynamic perturbation of the spacecraft environment on timescales of  $< 10 \text{ minutes}$ .

It was hypothesized that the observed long-duration potential perturbations are caused by slowly expanding charged clouds of debris inducing voltages on the FIELDS antennas. We

explored the feasibility of this hypothesis by adapting a model developed for laboratory hypervelocity dust impacts to PSP data. Agreement was found between the data and model for voltage perturbation shapes and duration. For total debris-cloud charge, agreement between the model and estimates based on WISPR data analysis can be achieved for a physically reasonable collisional fragmentation power-law index and minimum fragment size. The model best-fit cloud expansion rate is poorly constrained by the available data. Even with these limitations, it was demonstrated that this hypothesis is potentially feasible.

Dust impacts on PSP provide a unique, if unintentional, active experiment that can be used to probe how impacts with high kinetic energy perturb scientific measurements and spacecraft operation, and how they can be used to probe both the acceleration of and plasma waves driven by newly created plasma in the near-Sun solar wind.

The authors thank Brendan Gallagher of the Naval Research Lab Space Science Division for his work assigning data quality flags to the WISPR data. The authors thank the PSP, FIELDS, and WISPR teams. The FIELDS experiment on PSP was designed and developed under NASA contract NNN06AA01C. The Wide-Field Imager for PSP (WISPR) instrument was designed, built, and is now operated by the US Naval Research

Laboratory in collaboration with Johns Hopkins University/ Applied Physics Laboratory, California Institute of Technology/ Jet Propulsion Laboratory, University of Gottingen, Germany, Centre Spatiale de Liege, Belgium and University of Toulouse/ Research Institute in Astrophysics and Planetology. G.S. is supported by WISPR Phase-E funds. All data used here are publicly available on the FIELDS and WISPR data archives: <http://fields.ssl.berkeley.edu/data/>, <https://wispr.nrl.navy.mil/wisprdata>.

## Appendix

Table 1 lists all identified impact events that show long-duration potential perturbations, where the impact event was captured by a digital fields board (DFB) burst data collection. The Parker Solar Probe (PSP) orbit number, as well as the date and time of burst data collection start are listed for each event. The presence of natural wave attenuation and search coil-measured impulsive magnetic response is evaluated for each. When impulsive magnetic responses are observed, the magnitude of the peak response is listed.

Figure 13 shows additional examples of WISPR images with streak QF values  $\geq 8$ . The left four images show primarily linear streak trajectories, while the right four images are consistent with

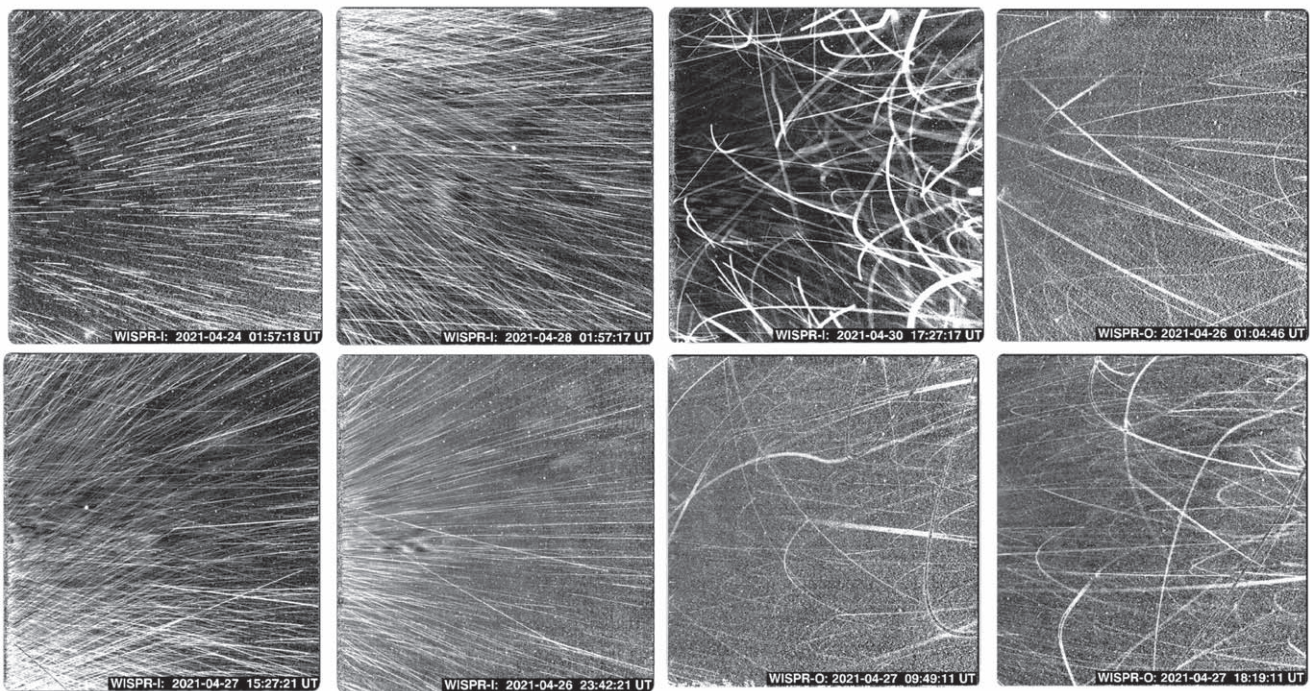


**Figure 13.** Examples of WISPR images with many streaks. The left four images show mostly linear streaks, and the right four images show curved streaks.

**Table 1**  
Impact Events with Long-duration Potential Perturbations Captured by Digital Fields Board Burst Data

Orbit #	Date/Time	Wave Attenuation	SCM Response
1	2018-11-04/00:10:29	Yes	Yes (~0.8 nT)
1	2018-11-04/03:16:14	Yes	Yes (~0.5 nT)
1	2018-11-05/00:33:15	Yes	Yes (~1.5 nT)
1	2018-11-06/17:22:44	No waves	No
1	2018-11-08/15:58:06	No waves	No
1	2018-11-08/16:03:09	No waves	No
1	2018-11-09/09:09:52	No waves	No
1	2018-11-10/00:43:23	No waves	Yes (~0.75 nT)
1	2018-11-10/03:33:05	No waves	No
1	2018-11-10/04:22:33	No waves	No
1	2018-11-10/14:41:40	No waves	Yes (~0.1 nT)
1	2018-11-11/13:54:54	No waves	No
2	2019-03-30/16:34:43	No waves	Yes (~0.5 nT)
2	2019-04-02/22:28:40	No waves	No
2	2019-04-04/01:13:17	Yes	Yes (~0.35 nT)
2	2019-04-06/02:21:12	No waves	No
2	2019-04-07/15:32:01	No waves	No
3	2019-08-26/20:18:20	No waves	No
3	2019-09-05/20:15:42	No waves	No
3	2019-09-06/12:33:59	No waves	No
3	2019-09-09/14:32:03	No waves	No
3	2019-09-09/19:18:07	No waves	No
3	2019-09-12/08:35:40	No waves	No
4	2020-01-29/02:34:13	Yes	No
4	2020-01-31/14:45:47	No waves	Yes (~4 nT)
4	2020-02-02/07:34:17	Yes	No
5	2020-06-09/09:01:17	No waves	No
5	2020-06-13/19:07:52	No waves	No
5	2020-06-13/19:58:15	No waves	No
6	2020-10-02/11:02:58	No waves	No
7	2021-01-20/08:19:56	No waves	No
7	2021-01-21/10:42:03	No waves	No
8	2021-04-22/11:10:00	No waves	No
8	2021-04-24/12:51:30	No waves	No
8	2021-04-25/19:39:00	No waves	No
8	2021-05-03/02:24:30	No waves	No

debris fragments traveling on curved trajectories. The WISPR camera and time stamp are indicated on each image.

### ORCID iDs

David M. Malaspina  <https://orcid.org/0000-0003-1191-1558>  
 Guillermo Stenborg  <https://orcid.org/0000-0001-8480-947X>  
 Doug Mehoke  <https://orcid.org/0000-0002-7698-2026>  
 Mitchell M. Shen  <https://orcid.org/0000-0002-3093-458X>  
 Hsiang-Wen Hsu  <https://orcid.org/0000-0002-5478-4168>  
 Kaushik Iyer  <https://orcid.org/0000-0002-1037-4730>  
 Stuart D. Bale  <https://orcid.org/0000-0002-1989-3596>  
 Thierry Dudok de Wit  <https://orcid.org/0000-0002-4401-0943>

### References

Bale, S. D., Goetz, K., Harvey, P. R., et al. 2016, *SSRv*, 204, 49  
 Benn, M., Jorgensen, J. L., Denver, T., et al. 2017, *GeoRL*, 44, 4701  
 Bernhardt, P. A., Roussel-Dupre, R. A., Pongratz, M. B., et al. 1987, *JGR*, 92, 5777

Collette, A., Meyer, G., Malaspina, D., & Sternovsky, Z. 2015, *JGRA*, 120, 5298  
 Davis, C. J., Davies, J. A., St., Cyr, O. C., et al. 2012, *MNRAS*, 420, 1355  
 Diaz-Aguado, M. F., Bonnell, J. W., Bale, S. D., et al. 2019, *JSpRo*, 56, 248  
 Diaz-Aguado, M. F., Bonnell, J. W., Bale, S. D., Wang, J., & Gruntman, M. 2021, *JGRA*, 126, e28688  
 Drolshagen, G., Dikarev, V., Landgraf, M., Krag, H., & Kuiper, W. 2008, *EM&P*, 102, 191  
 Ergun, R. E., Malaspina, D. M., Bale, S. D., et al. 2010, *PhPI*, 17, 072903  
 Fox, N. J., Velli, M. C., Bale, S. D., et al. 2016, *SSRv*, 204, 7  
 Garrett, H. B. 1981, *RvGSP*, 19, 577  
 Grun, E., Zook, H. A., Fechtig, H., & Giese, R. H. 1985, *Icar*, 62, 244  
 Gurnett, D. A., Anderson, R. R., Ma, T. Z., et al. 1986b, *JGR*, 91, 10013  
 Gurnett, D. A., Averkamp, T. F., Scarf, F. L., & Grun, E. 1986a, *GeoRL*, 13, 291  
 Gurnett, D. A., Grun, E., Gallagher, D., Kurth, W. S., & Scarf, F. L. 1983, *Icar*, 53, 236  
 Hess, P., Howard, R. A., Stenborg, G., et al. 2021, *SoPh*, 296, 94  
 Hooper, J. P. 2012, *JAP*, 112, 043508  
 Iyer, K., Poormon, K. L., Deacon, R., et al. 2013, *Procedia Eng.*, 58, 127  
 Iyer, K. A., Mehoke, D. S., & Batra, R. C. 2015a, *JSpRo*, 52, 584  
 Iyer, K. A., Mehoke, D. S., Chadegani, A., & Batra, R. C. 2015b, in *IEEE Aerosp. Conf. (Piscataway, NJ: IEEE)*, 1  
 Jorgensen, J. L., Benn, M., Connerney, J. E. P., et al. 2021, *JGRE*, 126, e06509  
 Joyce, C. J., Smith, C. W., Isenberg, P. A., et al. 2012, *ApJ*, 745, 112  
 Kellogg, P. J., Goetz, K., & Monson, S. J. 2016, *JGRA*, 121, 966  
 Laakso, H., Grard, R., Pedersen, A., & Schwelm, G. 1989, *AdSpR*, 9, 269  
 Lai, S. T., Murad, E., & McNeil, W. J. 2002, *JSpRo*, 39, 106  
 Langevin, Y., & Arnold, J. R. 1977, *AREPS*, 5, 449  
 Lee, N., Close, S., Lauben, D., et al. 2012, *IJIE*, 44, 40  
 Malaspina, D. M., Ergun, R. E., Bolton, M., et al. 2016, *JGRA*, 121, 5088  
 Malaspina, D. M., Halekas, J., Bercic, L., et al. 2020b, *ApJS*, 246, 21  
 Malaspina, D. M., Horányi, M., Zaslavsky, A., et al. 2014, *GeoRL*, 41, 266  
 Malaspina, D. M., Szalay, J. R., Pokorný, P., et al. 2020a, *ApJ*, 892, 115  
 Mann, I., Meyer-Vernet, N., & Czechowski, A. 2014, *PhR*, 536, 1  
 Mann, I., Nouzák, L., Vaverka, J., et al. 2019, *Ann. Geophys. Discuss.*, 2019, 1  
 McDermott, K. H., Price, M. C., Cole, M., & Burchell, M. J. 2016, *Icar*, 268, 102  
 Meyer-Vernet, N., Maksimovic, M., Czechowski, A., et al. 2009, *SoPh*, 256, 463  
 Moncuquet, M., Meyer-Vernet, N., Issautier, K., et al. 2020, *ApJS*, 246, 44  
 Nicholson, D. R. 1983, *Introduction to Plasma Theory* (1st; New York: Wiley)  
 Nishida, M., Hayashi, K., Nakagawa, J., & Ito, Y. 2012, *IJIE*, 42, 37  
 Nouzák, L., Hsu, S., Malaspina, D., et al. 2018, *P&SS*, 156, 85  
 O'Shea, E., Sternovsky, Z., & Malaspina, D. M. 2017, *JGRA*, 122, 11864  
 Pulupa, M., Bale, S. D., Bonnell, J. W., et al. 2020, *ApJS*, 246, 51  
 Pulupa, M., Bale, S. D., Bonnell, J. W., et al. 2017, *JGRA*, 122, 2836  
 Pusack, A., Malaspina, D. M., Szalay, J., et al. 2021, *PSJ*, 2, 186  
 Rival, M., & Mandeville, J. C. 1999, *Space Debris*, 1, 45  
 Sedlak, J. E., & Vint, B. 2018, *AAS/AIAA Astrodynamics Spec. Conf. GSFC-E-DAA-TN60168*, <https://ntrs.nasa.gov/citations/20180007809>  
 Shen, M.-H. 2021, PhD Thesis, Univ. of Colorado, Boulder  
 Shen, M. M., Sternovsky, Z., Garzelli, A., & Malaspina, D. M. 2021a, *JGRA*, 126, e29645  
 Shen, M. M., Sternovsky, Z., Horányi, M., Hsu, H.-W., & Malaspina, D. M. 2021b, *JGRA*, 126, e28965  
 St. Cyr, O. C., Kaiser, M. L., Meyer-Vernet, N., et al. 2009, *SoPh*, 256, 475  
 Szalay, J. R., Pokorný, P., Bale, S. D., et al. 2020, *ApJS*, 246, 27  
 Szalay, J. R., Pokorný, P., Malaspina, D. M., et al. 2021, *PSJ*, 2, 185  
 Trucano, T. G., Grady, D. E., & McGlaun, J. M. 1989, *IJIE*, 10, 587  
 Tsurutani, B. T., Clay, D. R., Zhang, L. D., et al. 2003, *GeoRL*, 30, 2134  
 Vaverka, J., Nakamura, T., Kero, J., et al. 2018, *JGRA*, 123, 6119  
 Vourlidis, A., Howard, R. A., Plunkett, S. P., et al. 2016, *SSRv*, 204, 83  
 Williams, T. W., Shulman, S., Sedlak, J., Ottenstein, N., & Lounsbury, B. 2016, in *AIAA/AAS Astrodynamics Spec. Conf. 2016-5675* (Reston, VA: AIAA)  
 Ye, S. Y., Averkamp, T. F., Kurth, W. S., et al. 2020, *JGRE*, 125, e06367  
 Ye, S. Y., Kurth, W. S., Hospodarsky, G. B., et al. 2018, *JGRA*, 123, 4952  
 Zaslavsky, A. 2015, *JGRA*, 120, 855  
 Zaslavsky, A., Meyer-Vernet, N., Mann, I., et al. 2012, *JGRA*, 117, A05102  
 Zhou, F., Molinari, J.-F., & Ramesh, K. T. 2006, *IJFr*, 139, 169